NEUROSCIENCE

Hierarchy in sensory processing reflected by innervation balance on cortical interneurons

Guofen Ma[1†], Yanmei Liu[1†], Lizhao Wang[1], Zhongyi Xiao[2], Kun Song[2], Yanjie Wang[1], Wanling Peng[2], Xiaotong Liu[2], Ziyue Wang[1], Sen Jin[3], Zi Tao[2], Chengyu T. Li[2,4], Tianle Xu[1,4], Fuqiang Xu[3], Min Xu[2,4]*, Siyu Zhang[1,4]*

Sensory processing is subjected to modulation by behavioral contexts that are often mediated by long-range inputs to cortical interneurons, but their selectivity to different types of interneurons remains largely unknown. Using rabies-virus tracing and optogenetics-assisted recording, we analyzed the long-range connections to various brain regions along the hierarchy of visual processing, including primary visual cortex, medial association cortices, and frontal cortices. We found that hierarchical corticocortical and thalamocortical connectivity is reflected by the relative weights of inputs to parvalbumin-positive (PV^+) and vasoactive intestinal peptide–positive (VIP^+) neurons within the conserved local circuit motif, with bottom-up and top-down inputs preferring PV^+ and VIP^+ neurons, respectively. Our algorithms based on innervation weights for these two types of local interneurons generated testable predictions of the hierarchical position of many brain areas. These results support the notion that preferential long-range inputs to specific local interneurons are essential for the hierarchical information flow in the brain.

INTRODUCTION

Sensory processing in the neocortex is modulated by behavioral contexts via activation of cortical interneurons. In an increasingly accepted scheme, cortical interneurons can be grouped into three genetically defined top-level classes [parvalbumin positive (PV^+), somatostatin positive (SST^+), and vasoactive intestinal peptide–positive (VIP^+)] (*1*, *2*). These top-level classes form conserved circuit motifs to enable rich and rapid modulations in local circuits (*3*–*7*). Furthermore, each class receives distinct long-range inputs and serves different functions in modulating sensory processing (*8*–*11*). For example, bottom-up corticocortical (CC) inputs from primary to secondary sensory cortex and thalamocortical (TC) inputs from relay nuclei activate PV^+ neurons to sharpen the sensory response and increase the temporal resolution (*12*–*15*). In addition, top-down CC inputs activate VIP^+ neurons to enhance sensory responses in the somatosensory (SS) and visual (VIS) cortex (*5*, *16*). Thus, long-range projections selectively recruit different local interneurons to shape sensory processing in sensory cortices.

Functionally, the sensory systems are hierarchically organized. In the visual system, higher-level areas pool information over multiple low-level areas to make behavior-related modulations of visual processing (*17*–*23*). To fully understand how behavioral contexts modulate visual processing through long-range projections, it is crucial to delineate the brain-wide connections to different types of neurons in cortical areas at various hierarchical stages. Although brain-wide connectivity without cell-type specificity is available (*24*–*26*), whole-brain inputs to different types of cortical interneurons remain to be fully characterized. Using rabies virus (RV)–assisted mapping (*27*), we systematically characterized the whole-brain inputs to the three top-level classes of cortical interneurons (PV^+, SST^+, and VIP^+ neurons) at different hierarchical stages of visual processing—the primary VIS, medial association cortices [posterior parietal (PTLp) cortex and retrosplenial (RSP) cortex], and frontal cortices [cingulate (ACA) cortex, orbitofrontal (ORB) cortex, and prelimbic/infralimbic (PL/ILA) cortex]. Furthermore, we investigated the link between the hierarchical directionality of long-range inputs and the input patterns of local interneurons. Since the cortical areas examined in the current study belong to the visual, medial, and prefrontal modules with well-accepted intermodule hierarchy (prefrontal > medial > visual) (*4*, *26*, *28*), the intermodule CC inputs across these modules were considered as well-defined bottom-up and top-down inputs. We found that the well-defined bottom-up and top-down CC inputs preferentially activated PV^+ and VIP^+ neurons, respectively. On the basis of these results, we built a model to classify the directionality of other long-range CC and TC inputs and generated testable predictions of hierarchical positions for cortical and thalamic areas.

In addition to connectivity mapping, we have used optogenetics-assisted electrophysiological recording to examine the synaptic properties of major CC and TC inputs to cortical interneurons. Since VIP^+ neurons are mainly distributed in L2/3 across different cortical areas (*4*), we focused on comparing synaptic properties of different types of interneurons in L2/3. These results validated the interneuron preferences of hierarchically organized long-range connections and further revealed differences in synaptic dynamics in a manner dependent on the input source and interneuron type. Thus, our results uncover general principles of innervation patterns to cortical interneurons for bottom-up and top-down connections and provide a basis for understanding the distinct roles of long-range inputs within the hierarchical organization in the brain.

[1]Center for Brain Science of Shanghai Children's Medical Center, Department of Anatomy and Physiology, Key Laboratory of Cell Differentiation and Apoptosis of the Chinese Ministry of Education, Shanghai Jiao Tong University School of Medicine, Shanghai 200025, China. [2]Institute of Neuroscience, CAS Center for Excellence in Brain Science and Intelligence Technology, State Key Laboratory of Neuroscience, Chinese Academy of Sciences, Shanghai 200031, China. [3]Brain Cognition and Brain Disease Institute (BCBDI), Shenzhen Institutes of Advanced Technology, Chinese Academy of Sciences, Shenzhen-Hong Kong Institute of Brain Science-Shenzhen Fundamental Research Institutions, Shenzhen 518055, China. [4]Shanghai Research Center for Brain Science and Brain-Inspired Intelligence, Shanghai 201210, China.
*Corresponding author. Email: mxu@ion.ac.cn (M.X.); zhang_siyu@sjtu.edu.cn (S.Z.)
†These authors contributed equally to this work.

RESULTS

Whole-brain mapping of long-range connections to cortical interneurons

To identify the long-range inputs to different types of cortical interneurons in the visual network, we used RV-mediated retrograde mapping, which labels monosynaptic inputs to selected interneurons (starter cells) with high specificity (*27*). Avian-specific retroviral receptor (TVA), red fluorescent protein (mCherry), and rabies glycoprotein (RG) were expressed in cortical interneurons by injecting Cre-inducible adeno-associated virus (AAVs) into the cortical areas (VIS, PTLp, RSP, ACA, ORB, and PL/ILA) of PV-, SST-, and VIP-Cre mice. Two to three weeks later, we injected a modified RV-expressing enhanced green fluorescent protein (EGFP) (RV-ΔG-EGFP+EnvA), which only infects cells expressing TVA and requires RG to spread retrogradely to presynaptic cells (Fig. 1A and fig. S1). After histological sectioning and fluorescence imaging, each brain sample was aligned to the Allen Mouse Brain Atlas (*29*) to facilitate three-dimensional (3D) whole-brain visualization and quantitative analyses. An atlas rotation module was added into our software package (*30*) to allow the 3D rotation of the reference atlas by arbitrary angles to fit each sample (Fig. 1B; see also Materials and Methods). The RV-labeled neurons were then detected and registered in the reference atlas (see table S1 for anatomical abbreviations). To facilitate data retrieval, we also used an interactive sunburst diagram to represent the whole-brain distribution of labeled inputs (http://top-down-network.org/).

Across brain samples, the starter cells (expressing both mCherry and EGFP) were distributed throughout the cortical layers over large portions of each cortical area (figs. S2 and S3). Most of the starter cells were located in the target areas (88 ± 1%, $n = 83$ mice), with a few cells spreading into the adjacent cortical areas. Most PV^+ and SST^+ starter cells were found in L2/3 and L5, whereas VIP^+ starter cells were mainly detected in L2/3 (fig. S2 and table S2). The layer patterns of starter cells were largely consistent with the distribution of these interneurons (see also fig. S4 and table S2) (*4*). We calculated the number of input neurons per starter cell for each animal across all groups with different injection sites. In each group, the input/starter cell ratios are similar for three types of interneurons [$P > 0.7$, two-way mixed analysis of variance (ANOVA)]. However, the input/starter cell ratio is significantly larger in VIS, RSP, PTLp, and ACA groups than in ORB and PL/ILA groups ($P < 0.05$, post hoc pair-wise Tukey's tests), indicating the region specificity of input/starter cell ratio (fig. S5).

Trans-synaptically labeled presynaptic neurons (expressing EGFP only) were found in multiple cortical and subcortical regions (movies S1 to S6). Reconstructing and superimposing the locations of presynaptic neurons in PV-, SST-, and VIP-Cre mice revealed extensive overlap in their spatial distributions (fig. S6). The number of labeled neurons varied across brains. To make each brain equally weighted in the population average, the input percentage from each region was quantified by dividing the number of labeled neurons found in that region by the total number of labeled neurons detected in the entire brain, with the exception of the injection site. We constructed a quantitative brain-wide input matrix for cortical interneurons (Fig. 1, C and D; see table S1 for the underlying values; interactive sunburst diagram at http://top-down-network.org/). In this matrix, the input percentage span a greater than 10^4-fold range across the brain, indicating that quantitative description of the connectivity needs to be considered for understanding the organization of neural network.

Hierarchical CC connectivity reflected by innervation pattern on interneurons

The trans-synaptic retrograde tracing has shown that the local interneurons shared all the major long-range inputs with biased input percentages. The absolute majority of the presynaptic neurons were found to lie within the isocortex, followed by the thalamus (fig. S3). We thus focused our analyses on the CC and TC inputs. Since the visual network consists of the cortical areas in visual, medial, and prefrontal modules and its hierarchical organization predicted the direction of information flow (*4*, *26*, *28*), we examined whether the cortical hierarchy is linked to the input pattern on local interneurons. To understand the relationship between the directionality of CC inputs and their input patterns on different types of interneurons quantitatively, we used the anatomical data from well-defined bottom-up and top-down CC inputs across different modules to train a support vector machine (SVM) classifier. We found that only the combination of input percentages to PV^+ and VIP^+ neurons accurately predicted the directionality of intermodule CC inputs (Fig. 2, A to C). In contrast, the input patterns of all other cell-type combinations failed to separate well-defined bottom-up and top-down inputs (Fig. 2C). These results indicated that the link between the hierarchy and input patterns is specifically reflected in the relative weights of innervation on PV^+ and VIP^+ neurons.

We thus defined the hierarchy index ($HI_{ANATOMY}$) for each inter-region connectivity by comparing its input percentages to PV^+ and VIP^+ neurons (Fig. 2D and Eq. 1 in Materials and Methods). Well-defined bottom-up inputs show negative $HI_{ANATOMY}$ values, in contrast to the positive $HI_{ANATOMY}$ values observed in well-defined top-down inputs. The SVM classifier trained with the $HI_{ANATOMY}$ values ($Classifier_{ANATOMY}$) revealed that the decision boundary for classification of bottom-up and top-down inputs is close to 0 (boundary = −0.018), suggesting that the sign of $HI_{ANATOMY}$ can be used to predict the directionality of a specific input. Notably, the reciprocal connections between the cortical areas in each module show opposite preferences for PV^+ and VIP^+ neurons in most cases in the visual network, indicating opposite hierarchical directions of these inputs.

Furthermore, to evaluate the hierarchical position of cortical areas in the visual network, we computed the hierarchy score of each cortical area based on the reciprocal CC connections (*28*). The initial hierarchy score for each cortical area (as both a source and target) was defined as the averaged difference between the $HI_{ANATOMY}$ values of its outputs and inputs (Eq. 2 in Materials and Methods). The score of each area was then iterated on the basis of the current hierarchy scores of its targets and sources to further refine the hierarchy (Eqs. 3 and 4 in Materials and Methods; see also fig. S7). In this way, we obtained the hierarchical organization of cortical areas in the visual network (Fig. 2E).

Innervation pattern on interneurons for hierarchical TC connectivity

Thalamus is a major input source for cortex, and the laminar axon distribution patterns of hierarchically organized TC inputs obey similar rules as CC inputs (*28*). Thus, we hypothesized that the anatomical rules derived from the CC input patterns of interneurons could be used in TC inputs to predict their directionality. To simplify our model, we grouped the thalamic nuclei that provided major inputs (>0.5% for at least one interneuron class) in the ventral, lateral, anterior, medial, midline, and intralaminar groups (*29*), except the ones with known functions in visual processing [LGd, LP/LD,

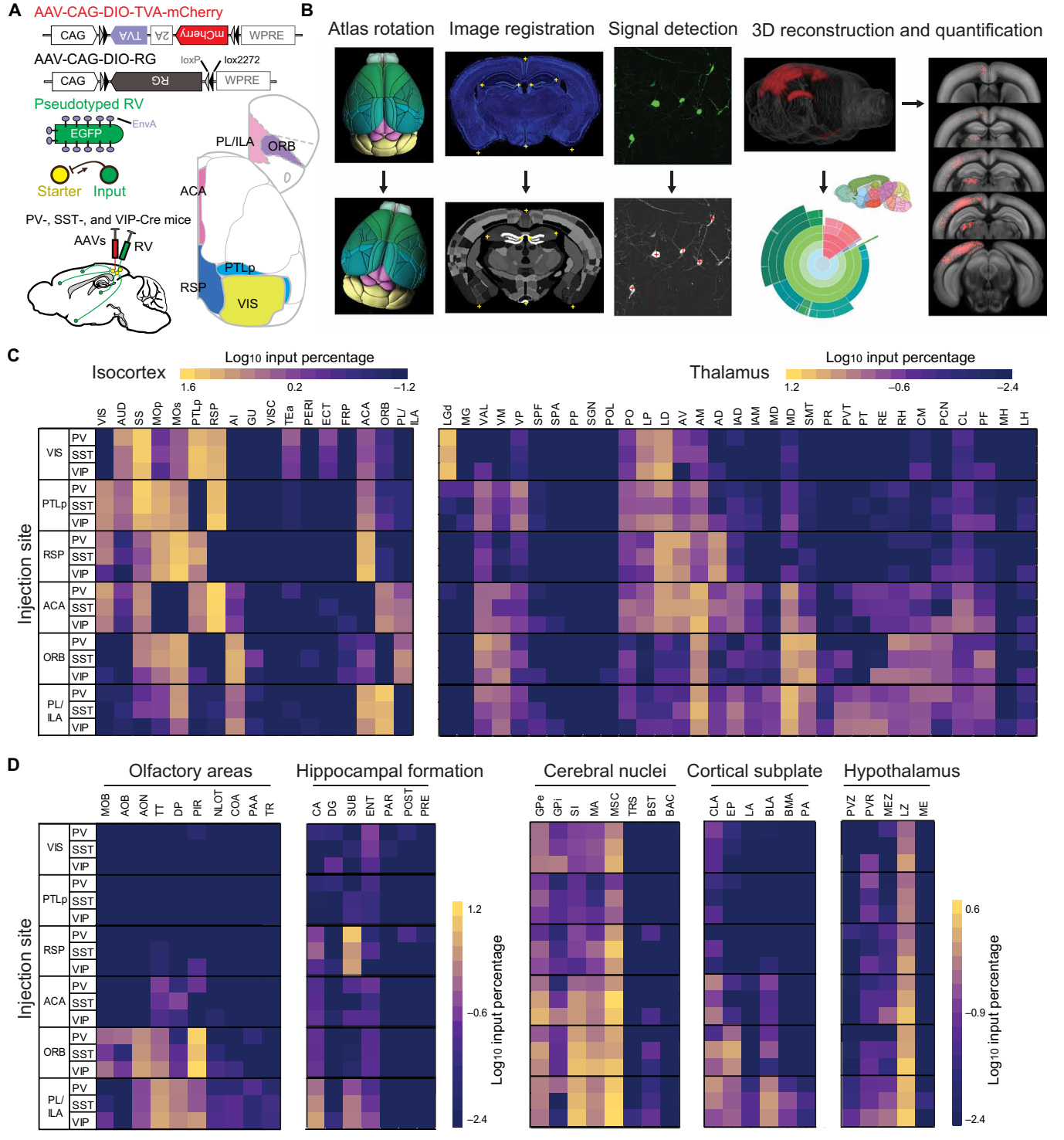

Fig. 1. RV-assisted brain-wide mapping of inputs to PV$^+$, SST$^+$, and VIP$^+$ neurons in VIS, PTLp, RSP, ACA, ORB, and PL/ILA. (**A**) Viral vectors and injection procedure for RV-mediated trans-synaptic retrograde tracing from different types of cortical interneurons. (**B**) Steps for data processing. In atlas rotation, Allen reference atlas was rotated to mimic the sectioning angle of the experimental brain. In image registration, the raw image (top) was mapped onto the corresponding coronal section of rotated reference atlas (bottom). In signal detection, retrogradely labeled neurons were identified manually (red crosses). In three-dimensional reconstruction and quantification, detected signals were projected to Allen reference atlas and quantified as the percentage of labeling in each brain region. (**C**) Matrixes show the input percentage of cortical areas (left) and thalamic nuclei (right) to VIS, PTLp, RSP, ACA, ORB, and PL/ILA in three mouse lines (PV-, SST-, and VIP-Cre; raw values in table S1). Each row contains the $\log_{10}$-transformed input percentage averaged from the experiments in one target region. Columns show cortical and thalamic input areas. The color map ranges from $10^{-1.2}$ to $10^{1.6}$ for cortex and from $10^{-2.4}$ to $10^{1.2}$ for thalamus. (**D**) Similar to (C), for the inputs from other subcortical areas. The color map ranges from $10^{-2.4}$ to $10^{1.2}$ for olfactory areas and hippocampal formation and from $10^{-2.4}$ to $10^{0.6}$ for cerebral nuclei, cortical subplate, and hypothalamus.

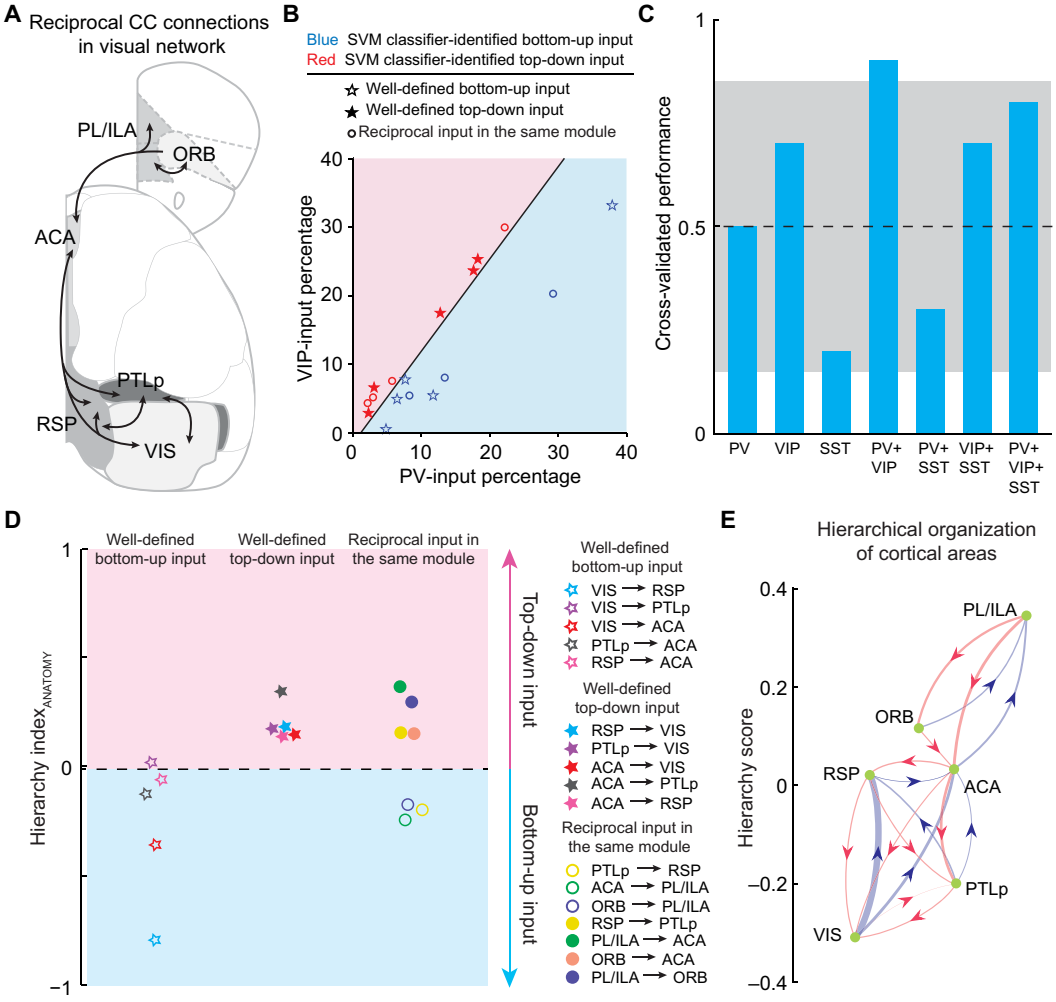

Fig. 2. Hierarchical organization of CC inputs. (**A**) Major reciprocal connections between the cortical areas in the visual network. Included are the connections with >2% input percentage for at least one interneuron type. (**B**) Decision boundary for the classification of bottom-up and top-down inputs derived from SVM classifier, which was trained with the input percentage to PV^+ and VIP^+ neurons in well-defined bottom-up and top-down CC inputs. (**C**) Cross-validated classifier performances on leave-one-out data, when different combinations of input-percentage information are used. Gray area indicates the 95% confidence interval of classifier performances on shuffled data. (**D**) Decision boundary for the classification of bottom-up and top-down inputs derived from $Classifier_{ANATOMY}$, which was trained with the $HI_{ANATOMY}$ of well-defined bottom-up and top-down CC inputs. (**E**) Network diagram showing the hierarchical organization of cortical areas derived from their reciprocal connections. Arrowhead denotes direction of each input. Red lines, top-down inputs; blue lines, bottom-up inputs; line width represents value of $HI_{ANATOMY}$.

and MD) (please see table S1 for a list of brain structure abbreviations)] (*19*, *31*, *32*). We calculated the $HI_{ANATOMY}$ of TC inputs by comparing their input percentages to PV^+ and VIP^+ neurons (Eq. 1 in Materials and Methods) and used the SVM classifier trained with CC inputs ($Classifier_{ANATOMY}$) to predict the directionality of TC inputs based on their $HI_{ANATOMY}$ values (Fig. 3, A and B).

To examine whether the TC connections affect the cortical hierarchy inferred by our algorithms, we computed the hierarchy score of each cortical and thalamic area based on both CC and TC connections (*28*). Similar to the algorithms described above, the initial hierarchy score for each cortical area was defined as the averaged difference between the $HI_{ANATOMY}$ values of its outputs and inputs, which consist of both CC and TC connections (Eq. 5 in Materials and Methods). In addition, since the thalamic area is always a source in TC connections, the initial hierarchy score for the thalamic area was defined as the averaged $HI_{ANATOMY}$ values of its outputs (Eq. 6 in Materials and Methods). To further refine the hierarchy, the scores of both cortical and thalamic areas were iterated until they converged to fixed values (Eqs. 7 to 9 in Materials and Methods). We then compared the hierarchy constructed from both CC and TC connections with that obtained using only CC connections. First, we found that the cortical and thalamic areas in the visual network were significantly hierarchically organized, because the observed global hierarchy scores were significantly higher than the scores from shuffled connections in both versions of hierarchy ($P < 8 \times 10^{-51}$, Wilcoxon rank-sum test; Fig. 3C). Second, these two versions of hierarchy had similar global hierarchy scores, and adding TC connections did not change the ranking of cortical areas in the visual network (Fig. 3, C and D). This indicates that TC connections provided similar hierarchical information to CC connections. The hierarchical organization of the visual network, based on the computational studies of CC and TC connections, is summarized by the diagram in Fig. 3E.

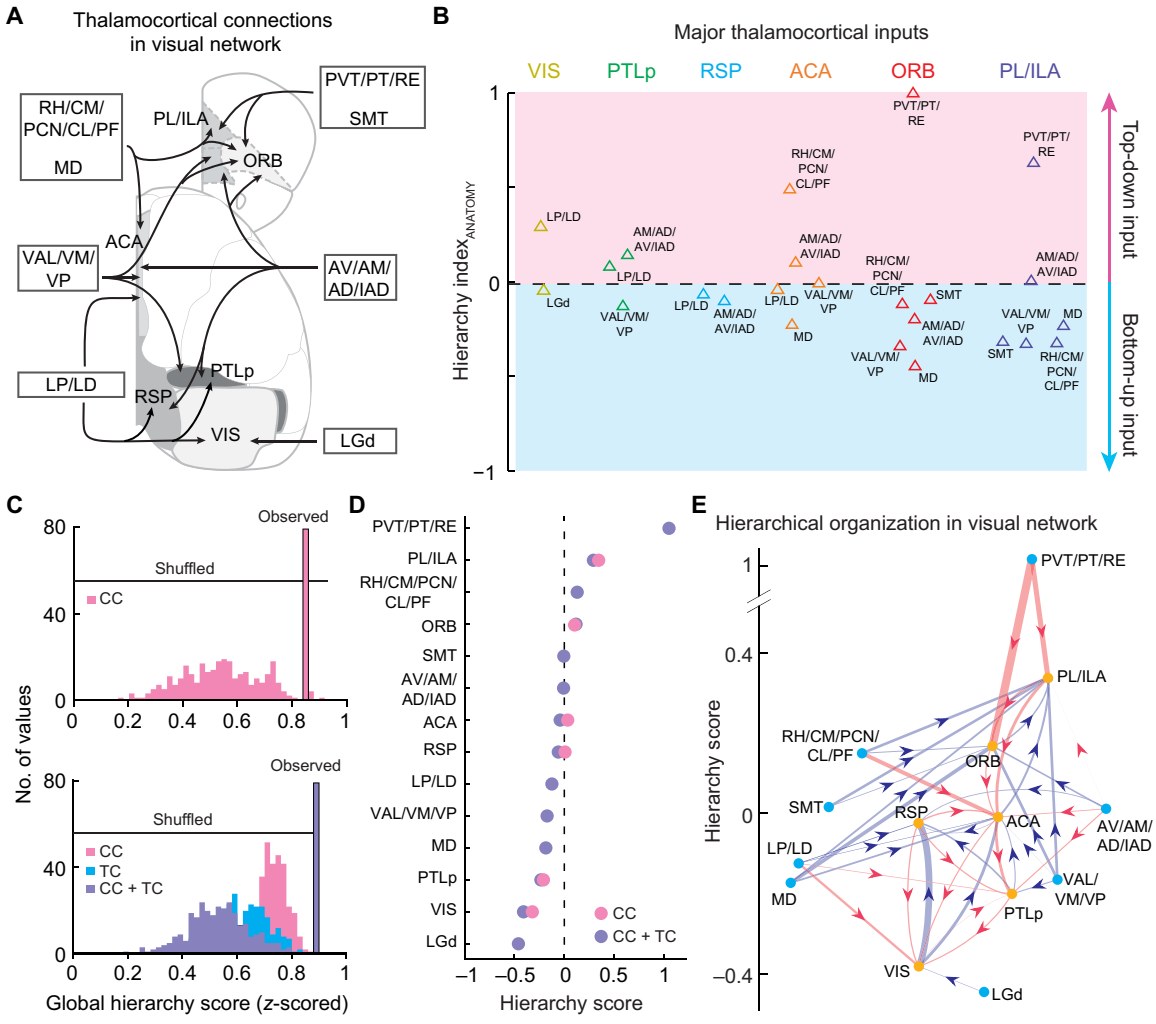

Fig. 3. Hierarchical organization of TC inputs. (**A**) Major thalamic inputs to the cortical areas in the visual network. Included are the connections with >0.5% input percentage for at least one interneuron class. (**B**) TC inputs classified by $Classifier_{ANATOMY}$. The decision boundary is the same as in Fig. 2D. (**C**) Global hierarchy scores for CC connections only (top) and the scores when both CC and TC connections are included (bottom). Scores for the observed data are shown as single outlined bars. Distributions of hierarchy scores were obtained from shuffled datasets ($n = 300$). Pink, CC; blue, TC; purple, CC + TC. (**D**) Hierarchy scores based on CC connections only (pink) or both CC + TC connections (purple). Cortical and thalamic areas are rank-ordered by their CC + TC hierarchy scores. (**E**) Network diagram showing the hierarchical organization in the visual network. Yellow dots, cortical areas; blue dots, thalamic areas. Arrowhead denotes direction of each input. Red lines, top-down inputs; blue lines, bottom-up inputs; line width represents value of $HI_{ANATOMY}$.

To further examine the consistency of the information provided by TC and CC connections, we computed the hierarchy score of each cortical and thalamic area based on only TC connections. The initial hierarchy score for each cortical area was defined as the averaged $HI_{ANATOMY}$ values of its TC inputs, and the initial hierarchy score for the thalamic area was defined as the averaged $HI_{ANATOMY}$ values of its outputs (Eqs. 10 and 11 in Materials and Methods). Next, the scores of both cortical and thalamic areas were iterated until they converged (Eqs. 12 to 14 in Materials and Methods). In this version of hierarchy, the ranking of cortical and thalamic areas was broadly similar to that derived from CC and TC connections (fig. S8), and the correlation between these two hierarchical networks are very high [Pearson's correlation coefficient (r) = 0.98, $P = 5 \times 10^{-10}$]. These results further strengthened the notion that the information provided by TC connections is consistent with CC connections, thus resulting in robust hierarchies. Together, these results uncovered a unifying rule of input patterns on local interneurons for the hierarchical organization across the cortex and thalamus.

Synaptic properties of long-range CC connections

RV tracing is a powerful tool for visualizing the distribution of inputs to specific neuronal populations but lacks the information about the synaptic properties of labeled connections. However, the synaptic strength and dynamics are crucial for understanding the function of a specific input. Thus, we used optogenetics-assisted electrophysiological recording to further investigate the synaptic properties of major long-range inputs revealed by RV tracing. We focused on comparing synaptic properties of different types of interneurons in L2/3, because VIP^+ neurons are mainly distributed in L2/3 across different cortical areas (see also fig. S4 and table S2) (*4*). First, we measured the strength and dynamics of well-defined bottom-up and top-down CC inputs across different modules (*4*, *28*). To identify each

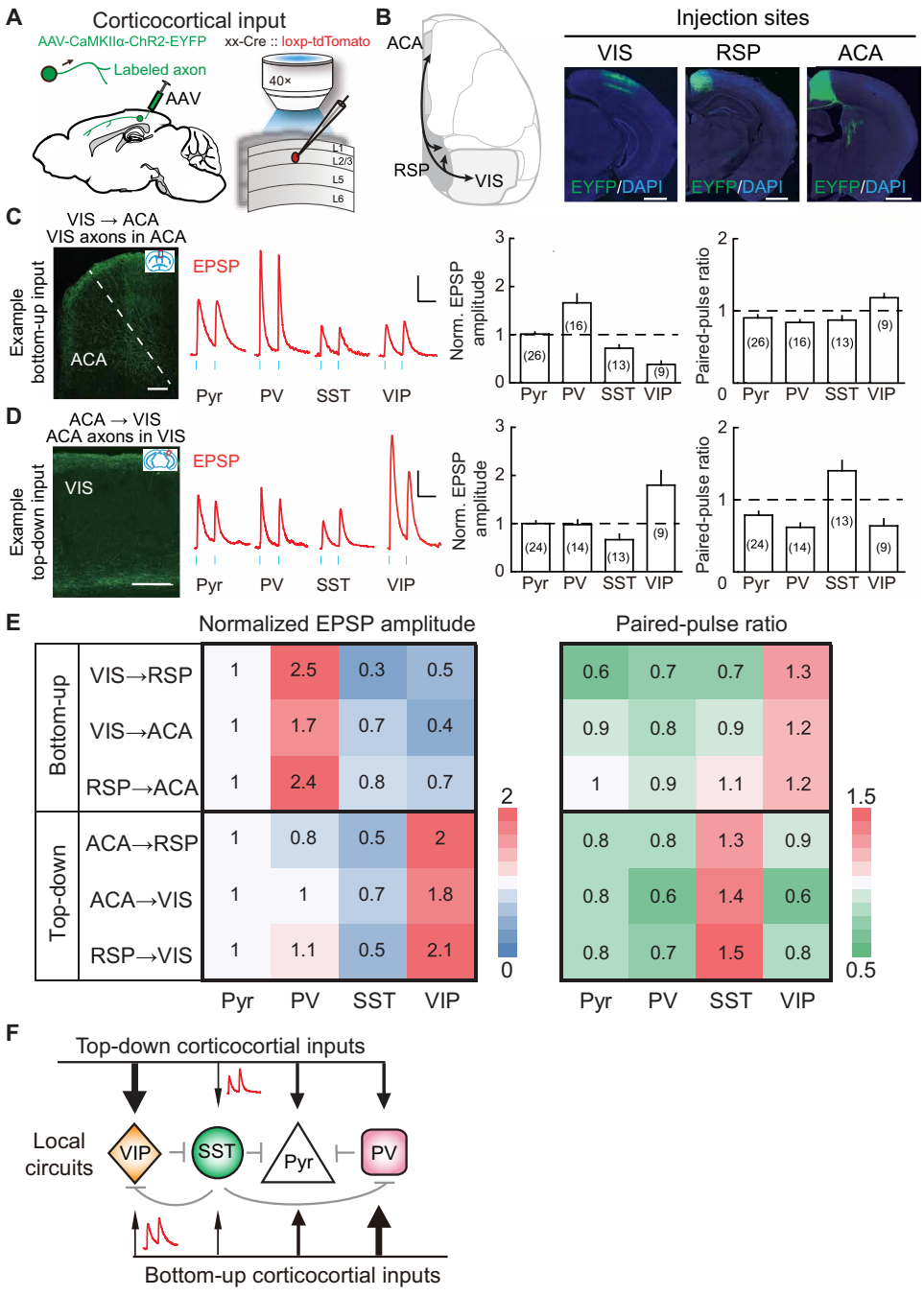

Fig. 4. Synaptic properties of well-defined bottom-up and top-down CC inputs. (**A**) Schematic of slice experiment. Viral vectors and injection procedure for expressing ChR2 in cortical pyramidal (Pyr) neurons (left). Whole-cell recording from different cell types in layer 2/3 and optogenetic activation of long-range inputs (right). (**B**) Schematic diagram and viral injection sites for examined inputs. Scale bars, 1 mm. (**C** and **D**) Synaptic properties of example bottom-up and top-down CC inputs. EPSP amplitude was normalized by Pyr-neuron response. Neuron numbers the shown in parentheses. (C) Synaptic properties of VIS → ACA inputs. Left: VIS axons (green) in ACA (red box in coronal diagram). Scale bar, 200 μm. Middle: Example blue light–evoked EPSPs recorded from Pyr, PV^+, SST^+, and VIP^+ neurons. Blue dots, 5-ms light stimulation (10 Hz). Scale bars, 0.1 s, 3 mV. Right: Normalized EPSP amplitude and paired-pulse ratio (PPR). EPSP amplitude in PV^+ neurons was larger than those in any other group ($P < 0.04$, Wilcoxon rank-sum test). PPR showed significant facilitation (PPR > 1) at the synapses onto VIP^+ neurons ($P = 0.02$, Wilcoxon signed-rank test) and depression (PPR < 1) onto other cell types ($P < 0.04$). Error bar, ±SEM. (D) Similar to (C), for ACA → VIS inputs. EPSP amplitude in VIP^+ neurons was larger than those in any other group ($P < 0.02$, Wilcoxon rank-sum test). PPR show significant facilitation at the synapses onto SST^+ neurons ($P = 0.02$) and depression onto other cell types ($P < 0.004$). (**E**) Matrix of normalized EPSP amplitude (left) and PPR (right) for well-defined bottom-up and top-down CC inputs. (**F**) Diagram of local circuits recruited by bottom-up and top-down CC inputs. Black lines, bottom-up/top-down connections; line width represents the amplitude of synaptic input. Red trace, schematic drawing of EPSPs for facilitating inputs. Gray lines, other known connections.

type of interneuron, we crossed PV-, SST-, and VIP-Cre mice with loxP-flanked tdTomato reporter mice. Channelrhodopsin-2 (ChR2) was expressed in excitatory cortical neurons using AAV–calcium/calmodulin-dependent protein kinase IIα (CaMKIIα)–hChR2(H134R)–enhanced yellow fluorescent protein (EYFP) (Fig. 4, A and B). Consistent with RV tracing results, we observed excitatory postsynaptic potentials (EPSPs) in all three types of interneurons evoked by optogenetic activation of long-range CC inputs. The EPSPs had short onset latencies (<3 ms) and were blocked by the antagonist of AMPA receptors [6-cyano-7-nitroquinoxaline-2,3-dione (CNQX; 10 μM); fig. S9], suggesting monosynaptic glutamatergic inputs from cortical areas. Although each input has different synaptic strength and dynamics, the following results revealed unique patterns correlated with the directionality of long-range inputs.

Bottom-up inputs (VIS → RSP, VIS → ACA, and RSP → ACA inputs) to PV^+ neurons exhibited the largest amplitude but rapid depression of synaptic potentials, whereas synapses onto VIP^+ neurons were initially weak in strength but showed synaptic facilitation (Fig. 4, C and E, and fig. S10, A and B). In contrast, top-down inputs (ACA → RSP, ACA → VIS, and RSP → VIS inputs) onto VIP^+ neurons were strongest but showed depression and those onto SST^+ neurons were initially weak but showed facilitation (Fig. 4, D and E, and fig. S10, C and D). Furthermore, these preferences in bottom-up inputs for PV^+ neurons and top-down inputs for VIP^+ neurons were observed even after local neuron spiking was blocked with tetrodotoxin (TTX) (fig. S11) (*33*), confirming the interneuron preference of monosynaptic inputs within the cortical hierarchy. Thus, well-defined bottom-up and top-down CC inputs preferentially recruit distinct types of local interneurons (Fig. 4F).

Next, we measured the synaptic properties of reciprocal CC connections in each module (Fig. 5, A and B, and figs. S10, E to K, and S12). Between the medial association cortices, PTLp→RSP input evoked the strongest response in PV^+ neurons, similar to the well-defined bottom-up inputs (Fig. 5C). In addition, RSP → PTLp input evoked the strongest response in VIP^+ neurons, similar to the top-down inputs. Among the frontal cortices, ACA → PL/ILA and ORB → PL/ILA inputs evoked the strongest response in PV^+ neurons, whereas ORB→ACA, PL/ILA → ACA, and PL/ILA → ORB inputs evoked the strongest response in VIP^+ neurons.

Last, we calculated the HI_{EPHYS} based on the synaptic strength of each input and trained the SVM classifier ($Classifier_{EPHYS}$) using the HI_{EPHYS} values of well-defined bottom-up and top-down CC inputs. $Classifier_{EPHYS}$ was further used to classify the directionality of the reciprocal CC connections in each module (Fig. 5D). Particularly, $Classifier_{EPHYS}$ separated the long-range CC inputs into two distinct groups, identical to that determined by $Classifier_{ANATOMY}$. These results indicated that the directionality of a specific input revealed by PV^+/VIP^+ input strength (physiology) is similar to the one revealed by PV^+/VIP^+ input percentage (anatomy). Moreover, we calculated the hierarchy score of cortical areas in the visual network based on the HI_{EPHYS} of CC connections (Fig. 5, E and F). This version of hierarchy provided a similar ranking of cortical areas and an increased global hierarchy score, further indicating the robustness of the hierarchy in the visual network.

Synaptic properties of TC connections

We next measured the synaptic strength and dynamics of TC inputs. Since the inputs from sensory relay nuclei to sensory cortices were extensively studied, we focused on the inputs from association nuclei (MD and LP/LD), which are known to be involved in visual processing (*19*, *31*, *32*, *34*). ChR2 was expressed in excitatory thalamic neurons by injecting AAV-CaMKIIα-hChR2(H134R)-EYFP into MD and LP/LD of PV-, SST-, and VIP-tdTomato mice (Fig. 6, A and B). Activation of the inputs from MD and LP/LD in each tested area evoked short-latency (~3 ms) glutamatergic EPSPs in all three interneuron classes (fig. S13).

Among cortical areas, MD only innervates frontal cortices (*24*, *25*, *32*). Activation of MD → ORB and MD → ACA inputs evoked the strongest response in PV^+ neurons, consistent with previous findings that MD provides potent feedforward inhibition to frontal cortices (*35*–*37*). MD inputs showed facilitation onto VIP^+ neurons and depression onto other neuronal types (Fig. 6, C and D, and fig. S14A). These synaptic properties of MD inputs to the frontal cortices are reminiscent of the bottom-up CC inputs described above, suggesting that MD may provide bottom-up modulation to information processing in the frontal cortices.

LP/LD are the only thalamic nuclei innervating cortical areas at all stages in the visual network (see also table S1) (*24*, *28*, *38*). The synaptic properties of LP/LD inputs changed markedly according to the target (Fig. 6D and fig. S14, B to D). Similar to bottom-up inputs, LP/LD → ACA input was strongest onto PV^+ neurons. On the contrary, LP/LD → VIS input was strongest onto VIP^+ neurons, consistent with top-down inputs. Notably, LP/LD → RSP input was strong on both PV^+ and VIP^+ neurons, exhibiting the characteristics of both bottom-up and top-down inputs. The dynamics of LP/LD inputs also varied at different hierarchical stages of visual processing. LP/LD → ACA and LP/LD → RSP inputs showed facilitation at the synapses onto VIP^+ neurons and depression or no clear change onto other neuronal types. LP/LD → VIS input showed depression onto all four neuronal types. These results suggested that LP/LD could differentially modulate visual processing at each stage by recruiting distinct classes of interneurons.

Last, we applied the $Classifier_{EPHYS}$, SVM classifier trained with the HI_{EPHYS} of CC inputs, to the TC inputs tested above. The $Classifier_{EPHYS}$ well separated the bottom-up and top-down TC inputs (Fig. 6E). LP/LD → RSP input is strong on both PV^+ and VIP^+ neurons and is thus close to the decision boundary. Together, our results on both CC and TC connections showed that the preference innervation pattern on PV^+ and VIP^+ neurons is a critical feature in the hierarchically organized network.

Synaptic dynamics linked to the directionality of CC and TC connections

To reveal the relationship between the directionality and the synaptic dynamics of CC and TC inputs, we examined the synaptic dynamics of bottom-up and top-down inputs identified by $Classifier_{EPHYS}$ (Fig. 7). We found that bottom-up CC inputs have significantly lower paired-pulse ratio (PPR) on SST^+ neurons and higher PPR on VIP^+ neurons than top-down CC inputs ($P < 0.03$, Wilcoxon rank-sum test; Fig. 7B). Similar to bottom-up CC inputs, bottom-up TC inputs showed short-term facilitation on VIP^+ neurons and depression on SST^+ neurons (Fig. 6 and fig. S14). However, unlike facilitating top-down CC inputs, the top-down TC input (LP/LD → VIS input) showed short-term depression on SST^+ neurons, similar to the TC input from high-order thalamic nuclei to the somatosensory cortex (POm → SS input) (*39*). These results suggested that the top-down TC and CC inputs may be different in recruiting SST^+ neurons. Furthermore, we used the synaptic-dynamics information

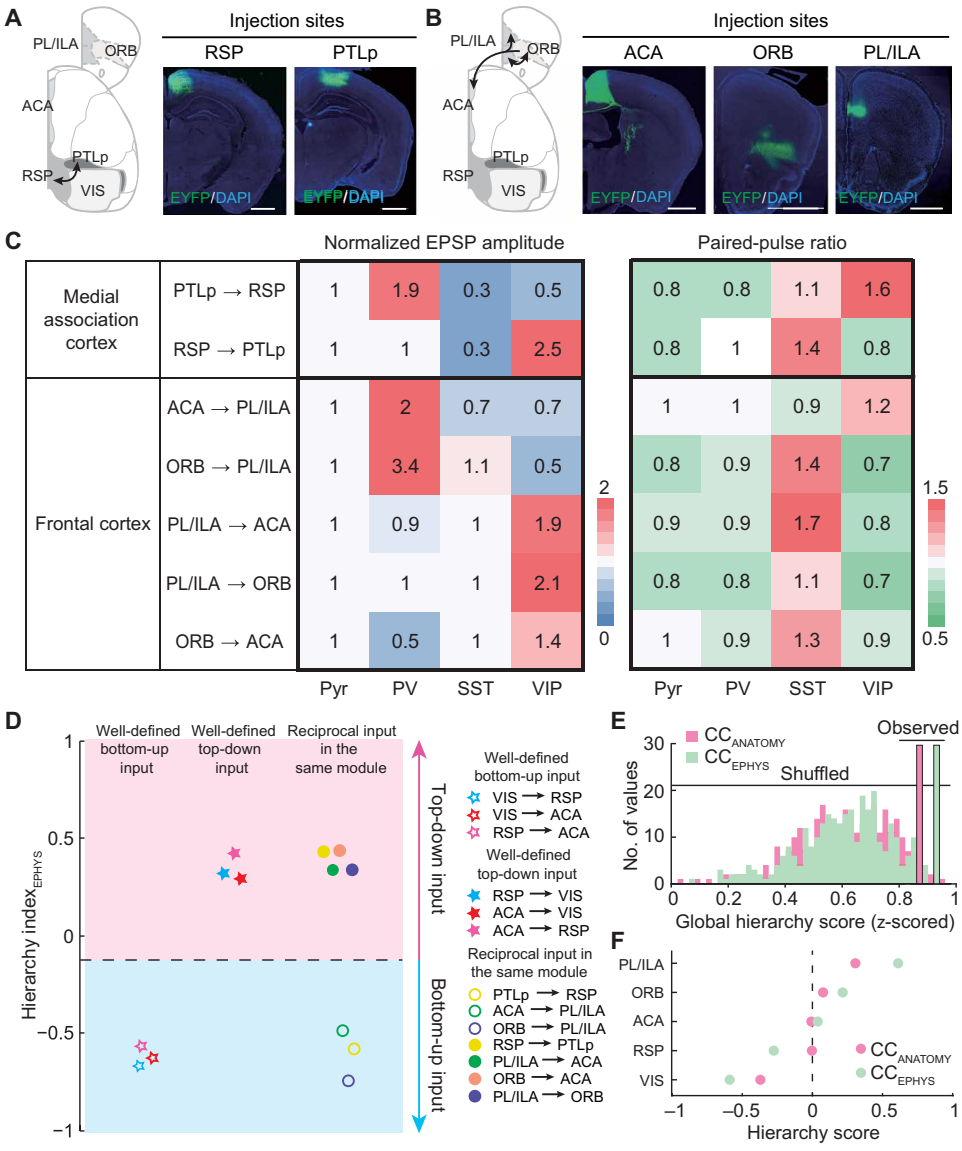

Fig. 5. Synaptic properties of reciprocal CC inputs in the same module. (**A** and **B**) Schematic diagram and viral injection sites for examined inputs. Scale bars, 1 mm. The image of RSP and ACA injection sites are the same as in Fig. 4. (**C**) Matrix of normalized EPSP amplitude (left) and PPR (right) for reciprocal CC inputs in the same module. EPSP amplitude was normalized by Pyr-neuron response. The PPR is measured by dividing the amplitude of the second EPSP into that of the first EPSP. (**D**) Decision boundary for the classification of bottom-up and top-down inputs derived from $Classifier_{EPHYS}$, trained with the HI_{EPHYS} of well-defined bottom-up and top-down CC inputs. (**E**) Global hierarchy scores for CC connections based on HI_{EPHYS} (green), compared to the scores based on $HI_{ANATOMY}$ (pink). (**F**) Hierarchy scores based on HI_{EPHYS} (green) or $HI_{ANATOMY}$ (pink) of CC connections. Included are the cortical areas with completed electrophysiological data of reciprocal connections. Cortical areas are rank-ordered by their $CC_{ANATOMY}$ hierarchy scores.

of both CC and TC inputs to train the SVM classifier and found that with a single-cell type, only the synaptic dynamics of VIP^+ neurons significantly correlated to the directionality (Fig. 7, C and D). Besides single-cell type, we also trained the SVM classifier with the synaptic dynamics of different cell-type combinations (fig. S15). Among all the different cell-type combinations, the SVM classifier trained with the synaptic dynamics of VIP^+ neurons ($Classifier_{VIP\text{-}PPR}$) is one of the best classifiers. The decision boundary revealed by $Classifier_{VIP\text{-}PPR}$ is close to 1 ($boundary_{VIP\text{-}PPR}$ = 1.05), indicating that for both CC and TC inputs, the bottom-up inputs are facilitating and the top-down inputs are depressing on VIP^+ neurons.

DISCUSSION

Using RV mapping and optogenetics-assisted electrophysiological recording, we systematically analyzed the long-range inputs to three top-level cortical interneuron classes (PV^+, SST^+, and VIP^+) at different hierarchical stages of visual processing. Our work provided a dataset describing the interneuron connectome with both anatomical and electrophysiological information at the cellular level. With the anatomical data, we obtained a unifying rule for the hierarchical organization of cortical and thalamic connections from their innervation patterns to cortical interneurons and further extended the study of these long-range connectivities with

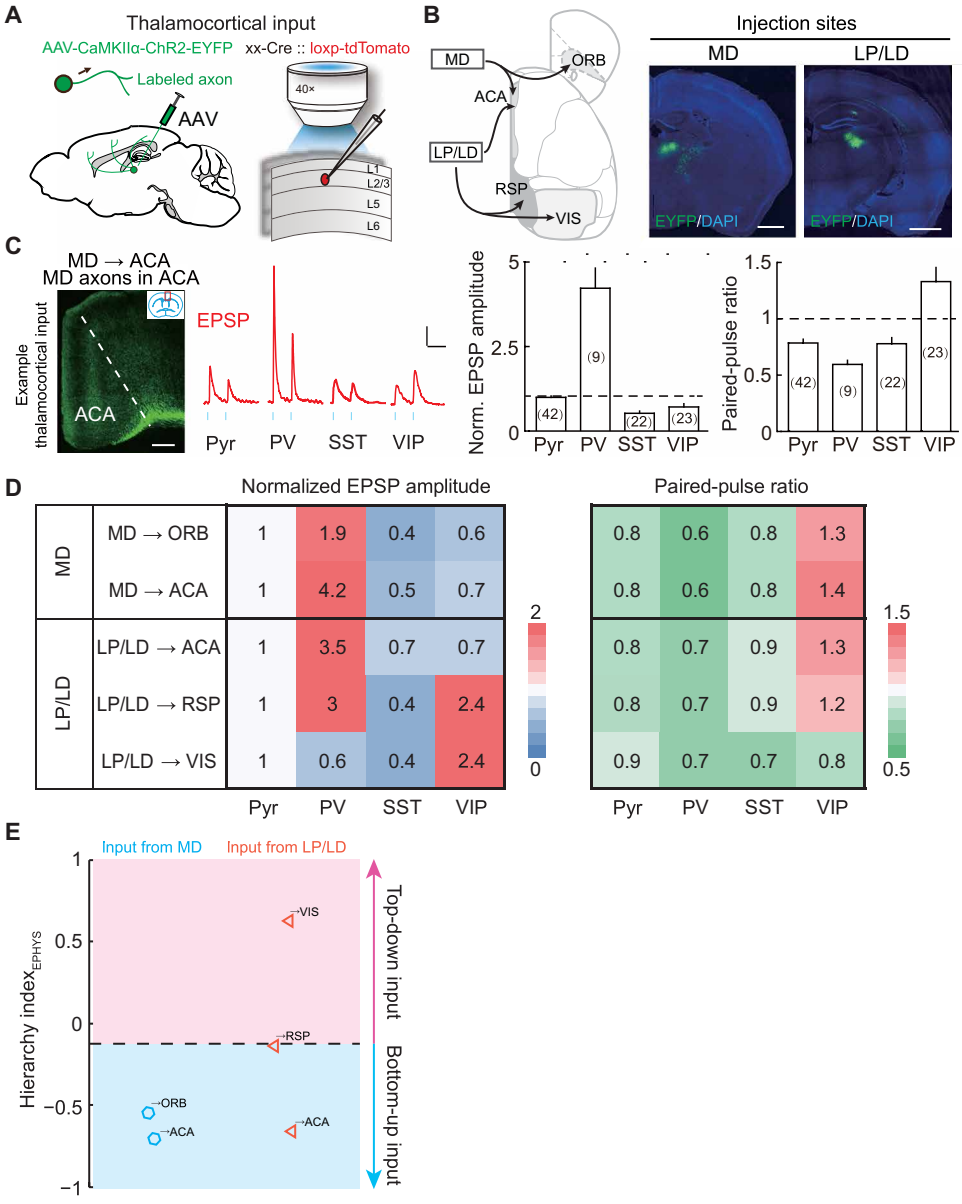

Fig. 6. Synaptic properties of TC inputs from association nuclei. (**A**) Schematic of slice experiment. Viral vectors and injection procedure for expressing ChR2 in thalamic neurons (left). Whole-cell recording from different cell types in layer 2/3 and optogenetic activation of TC inputs (right). (**B**) Viral injection sites for examined TC inputs. Schematic diagram of examined inputs (left). Viral injection sites in MD and LP/LD (right). Scale bars, 1 mm. (**C**) Synaptic properties of example TC inputs (MD → ACA). Left: MD axons (green) in ACA (red box in coronal diagram). EPSP amplitude was normalized by Pyr-neuron response. The PPR is measured by dividing the amplitude of the second EPSP into that of the first EPSP. Neuron numbers are shown in parentheses. Scale bar, 200 μm. Middle: Example blue light–evoked EPSPs recorded from Pyr, PV^+, SST^+, and VIP^+ neurons. Blue dots, 5-ms light stimulation (10 Hz). Scale bar, 0.1 s, 3 mV. Right, normalized EPSP amplitude and PPR. EPSP amplitude in PV^+ neurons was larger than those in any other group ($P < 8 \times 10^{-5}$, Wilcoxon rank-sum test). PPR shows significant facilitation (PPR > 1) at the synapses onto VIP^+ neurons ($P = 0.01$, Wilcoxon signed-rank test) and depression onto other cell types ($P < 0.004$). Error bar, ±SEM. (**D**) Matrix of normalized EPSP amplitude (left) and PPR (right) for TC inputs from association nuclei. (**E**) TC inputs classified by the $\text{Classifier}_{\text{EPHYS}}$. The decision boundary is the same as in Fig. 5D.

electrophysiological recording. Our results demonstrated a significant correlation between the hierarchically organized long-range CC and TC inputs and their innervation preference for local interneurons—bottom-up inputs favor PV^+ neurons, whereas top-down inputs prefer VIP^+ neurons.

The wiring diagram of cortical neurons is fundamental for their function. The brain-wide connectivity of the neocortex without cell-type specificity has been characterized by studies using anterograde and retrograde tracing (*24*–*26*). Recent studies also revealed the long-range input and output connections for cortical pyramidal neurons (*28*, *30*, *40*–*42*). However, the whole-brain connectivity for different types of cortical interneurons remains to be fully characterized. Using RV mapping, previous studies have obtained the brain-wide input maps for the three top-level interneuron classes in

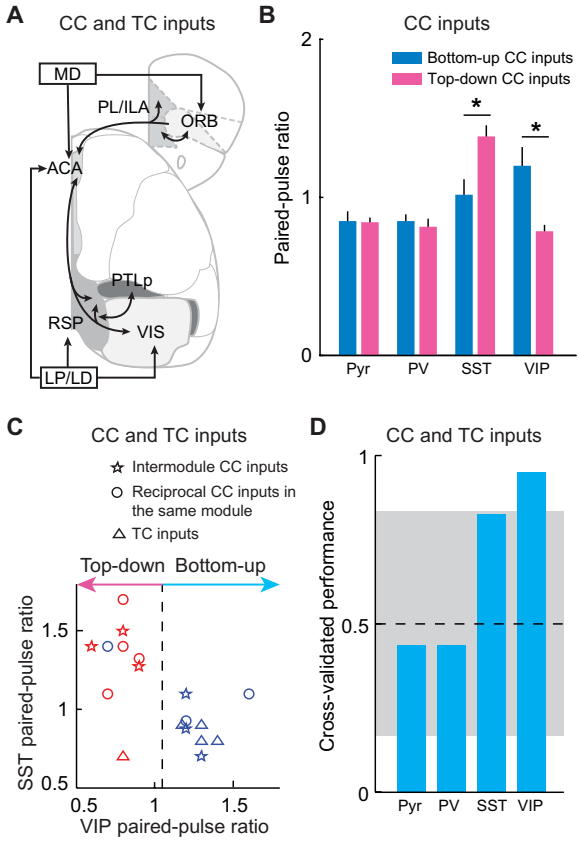

Fig. 7. The link between the directionality of long-range inputs and their synaptic dynamics. (**A**) Schematic diagram of examined CC and TC inputs. (**B**) PPR of CC inputs on different types of neurons. Bottom-up CC inputs have significantly lower PPR on SST$^+$ neurons and higher PPR on VIP$^+$ neurons than top-down CC inputs (*$P < 0.03$, Wilcoxon rank-sum test). Bottom-up inputs, $n = 6$; top-down inputs, $n = 7$. Error bar, ±SEM. (**C**) Decision boundaries (dashed lines) for the classification of bottom-up and top-down CC and TC inputs derived from SVM classifiers, trained with the PPR on VIP$^+$ neurons. Blue, bottom-up inputs classified by Classifier$_{EPHYS}$; red, top-down inputs classified by Classifier$_{EPHYS}$. (**D**) Cross-validated classifier performances on leave-one-out data, using the synaptic-dynamics information of CC and TC inputs on different types of neurons. Gray area indicates the 95% confidence interval of classifier performances on shuffled data.

individual cortical areas (AUD, SS, and mPFC) (*43*–*46*). Our study systematically analyzed the brain-wide inputs to cortical interneurons at different hierarchical stages of visual processing (Figs. 1 to 3). Using a linear machine learning classifier, we found that only the combination of PV$^+$/VIP$^+$ input percentage could separate well-defined bottom-up and top-down CC inputs. We then computed HI$_{ANATOMY}$ of each CC and TC input to compare the innervation difference on PV$^+$ and VIP$^+$ neurons and predicted the directionality of each input based on its HI$_{ANATOMY}$ value. Furthermore, we computed the hierarchy scores of the cortical and thalamic areas based on the HI$_{ANATOMY}$ value of their inputs and outputs. Adding TC inputs to the CC network did not change the hierarchical ranking of cortical areas and further increased the global hierarchy score. In addition, the hierarchical cortical and thalamic network inferred by only TC inputs is also similar to the one obtained from both CC and TC inputs (Pearson's $r = 0.98$). Thus, the hierarchical organization of TC inputs reflected by the input pattern of local interneurons followed the same rule as CC inputs.

The neocortex is a modular network (*4*, *26*, *28*) and its hierarchical organization predicts the direction of information flow. To construct a hierarchy in the network and measure its significance, we adapted the algorithms from Harris *et al.* (*28*). In particular, the hierarchy is constructed on the basis of the averaged connection directionality followed by iterations, and the significance of the obtained hierarchy is measured by global hierarchy scores. The main difference between our study and Harris's is that the directionality of each inter-areal connection is determined by its relative weights to PV$^+$ and VIP$^+$ neurons in our study, rather than laminar distribution patterns of axons in Harris's. We found that the hierarchy reflected by the input patterns of cortical interneurons is largely consistent with the one derived from laminar distribution patterns of axons in the mouse brain. In both versions of hierarchy, thalamic areas are found at the bottom and top, and the cortical and some thalamic areas are in the middle. The global hierarchy score (CC + TC) in the network we examined is 0.89, which is close to being perfectly hierarchical (1.00) and far from the median shuffled score (0.53) (Fig. 3C), indicating that these brain regions are highly hierarchically organized. Notably, the hierarchy constructed in our study works under the assumption that each input's HI value reflected the different levels of its directionality based on the innervation differences between PV$^+$ and VIP$^+$ neurons. The directionality levels of long-range inputs form a continuum between −1 and +1, with bottom-up and top-down inputs biased toward PV$^+$ and VIP$^+$ neurons, respectively. The hierarchy based on this assumption is robust since the rankings of brain areas are similar in the CC only, TC only, and CC + TC network. Moreover, when we removed this assumption by assigning −1 to bottom-up and +1 to top-down inputs, the hierarchy is still largely preserved, further indicating the robustness of the hierarchy in the visual network reflected by the innervation balance on interneurons. Besides the cortical areas within the medial and prefrontal modules in our study, higher visual areas in the visual module are also known to be hierarchically organized (*19*–*22*). Whether the input pattern on cortical interneurons in these areas also follows the rule described here remains to be studied.

Using optogenetics-assisted electrophysiological recording, we not only validated the interneuron preference revealed by RV tracing but also provided valuable information on synaptic dynamics that is dependent on the input source and interneuron type (Figs. 4 to 7). Bottom-up CC inputs on PV$^+$ neurons are strong and depressing, and those on VIP$^+$ neurons are initially weak but facilitating. By contrast, top-down CC inputs on VIP$^+$ neurons are strong and depressing, and those on SST$^+$ neurons are initially weak but facilitating. Thus, persistent bottom-up CC inputs may first recruit PV$^+$ neurons and then followed by VIP$^+$ neurons, whereas persistent top-down CC inputs may first recruit VIP$^+$ neurons and then SST$^+$ neurons in local circuits. Considering the temporal dynamics of sensory information processing at different stages, the activation of VIP$^+$ neurons by bottom-up and top-down CC inputs may thus be synergistic in removing dendritic inhibition of pyramidal neurons by suppressing SST$^+$ neurons (*3*, *5*–*7*), promoting top-down modulation in the visual network. This could be followed by activation of SST$^+$ neurons with repetitive top-down CC inputs and local excitatory inputs, which are also strongly facilitating (*47*), resulting in the inhibition of VIP$^+$ and PV$^+$ neurons and rebalance of the local network (*3*, *6*). In addition, the hierarchical TC inputs show similar

interneuron preference to CC inputs with slightly different synaptic dynamics. Both bottom-up CC and TC inputs have significantly higher PPR on VIP^+ neurons than top-down inputs. However, unlike the facilitating top-down CC inputs, top-down TC inputs are depressing on SST^+ neurons, suggesting that the top-down CC and TC inputs differentially recruit SST^+ neurons. These cell type–specific synaptic properties associated with the directionality of long-range inputs are important for understanding the information flow in the hierarchical neural network. In the current study, we focused on measuring the synaptic properties of long-range inputs onto L2/3 interneurons. The function of the hierarchically organized long-range inputs in other layers will require further investigation.

Besides the relatively conserved input patterns for PV^+ and VIP^+ neurons, we noticed more variations in the inputs onto SST^+ neurons. For example, the CC inputs across different hierarchical stages or between the medial association cortices are weak onto SST^+ neurons, in contrast to the strong inputs between the frontal cortices (similar to or even stronger than that onto pyramidal neurons). Considering the increased density of SST^+ neurons in the frontal cortices (*4*), they may play more important roles in information propagation between the frontal cortices. In addition, we found that TC inputs are always weak and depressing on SST^+ neurons, consistent with recent studies in the primary somatosensory cortex (*39*, *48*), indicating that SST^+ neurons are unlikely to be directly driven by TC inputs. Together, these results supported the diverse functions of SST^+ neurons in cortical information processing. Notably, learning can profoundly shape the neural circuits (*49*–*53*), e.g., visual experience facilitates top-down modulation and suppresses the bottom-up sensory drive to VIS, depending on the inactivation of SST^+ neurons (*54*). Whether this learning-induced modulation of the balance between top-down and bottom-up inputs happens along the hierarchy of sensory processing remains to be studied.

In the current study, we grouped the thalamic nuclei to simplify our model. However, it should be noted that even the thalamic nuclei with similar projection patterns may transfer different information to their target areas. For example, in animals performing a visual discrimination task, the neurons encoding visual and action information were found in both LP and LD, but the neurons encoding choice were only found in LD (*55*). The different roles of each thalamic nucleus in information processing need to be examined in more detail in the future. In addition, although optogenetics was widely used to investigate synaptic properties, due to technical limitations, e.g., different ChR2-expression levels in virally infected neurons, the synaptic release induced by optogenetic activation of axon terminals might differ from that evoked by action potentials. Action potential–evoked synaptic release of long-range inputs needs to be further investigated.

Although previous studies revealed several functional rules within the hierarchy of sensory processing (*9*, *19*, *22*, *23*, *56*), the function of hierarchically organized long-range inputs is still not fully understood. The top-level classes of interneurons were known to form conserved circuit motifs across cortical areas to dynamically suppressing excitation and enable rich and rapid modulations in local circuits (*3*–*7*). Recent studies have shown that the observed behavior-related modulation of cortical activity can only be generated with all three top-level classes of interneurons activated by long-range inputs (*46*, *57*, *58*). Our results indicated that hierarchically organized CC and TC inputs have distinct innervation patterns on local interneurons and thus determine the function of these long-range inputs in terms of how they interact with local circuits. Our anatomical and physiological characterization will be informative for future studies on more refined excitatory and inhibitory cell classification (*1*, *2*, *59*–*61*), which are likely to yield additional patterns of hierarchical connectivity. Besides cortical and thalamic inputs, sensory processing in the neocortex is also modulated by other subcortical long-range inputs, e.g., the neuromodulatory inputs (*62*–*64*). The dataset obtained in this study also included information on the innervation patterns on cortical interneurons from other subcortical regions that could be useful for future investigation of the role of these long-range inputs.

MATERIALS AND METHODS

Animals

Animal care and the experimental protocols were approved by the Animal Committee of Shanghai Jiao Tong University School of Medicine and the Animal Committee of the Institute of Neuroscience, Chinese Academy of Sciences. PV-, SST-, VIP-, and CaMKIIα-Cre and loxP-flanked tdTomato reporter mice (Jackson stock no. 017320, 013044, 010908, 005359, and 007909) were obtained from the Jackson laboratory. To visualize the interneurons, PV-, SST-, and VIP-Cre mice were crossed with the loxP-flanked tdTomato reporter mice. Male and female mice aged 5 to 24 weeks were used. Mice were housed in a 12-hour light/12-hour dark cycle (lights on at 07:00 a.m. and off at 07:00 p.m.) with free access to food and water.

Virus preparation

AAV preparation followed previously reported protocol (*30*). The AAV-CAG-DIO-TVA-mCherry, AAV-CAG-DIO-glycoprotein and AAV-CaMKIIα-hChR2(H134R)-EYFP vectors were from Addgene (plasmid nos. 48332, 48333, and 26969). AAV particles were produced by cotransfection of packaging plasmids into human embryonic kidney–293T cells, and cell lysates were fractionated by iodixanol gradient ultracentrifugation. Viral particles were desalted and concentrated with centrifugal filter (100 K). The genomic titer of AAV2-CAG-DIO-TVA-mCherry (2.1×10^{13} gc/ml), AAV2-CAG-DIO-glycoprotein (8.7×10^{12} gc/ml), and AAV-DJ-CaMKIIα-hChR2(H134R)-EYFP (8.1×10^{13} gc/ml) were determined by quantitative polymerase chain reaction (PCR). Glycoprotein-deleted (ΔG) and EnvA-pseudotyped RV (RV-ΔG-EGFP+EnvA) were used for retrograde monosynaptic tracing (*27*). RV-ΔG-EGFP+EnvA (2.4×10^8 IU/ml) were produced by BrainVTA.

Surgery

Adult mice were anesthetized with isoflurane (5% induction and 1.5% maintenance) and placed on a stereotaxic frame (Ruiwode Life Science). The temperature was kept at 37°C throughout the procedure using a heating pad. After asepsis, the skin was incised to expose the skull and the overlying connective tissue was removed. A craniotomy (~0.5 mm diameter) was made above the injection site. Viruses were loaded in a sharp micropipette mounted on a Nanoject II attached to a micromanipulator and then injected at a speed of 60 nl/min.

For retrograde monosynaptic tracing from cortical interneurons and pyramidal neurons, TVA receptor and RG, which are required for virus infection and trans-synaptic spread, respectively, were expressed in Cre-positive neurons by co-injection of AAV2-CAG-DIO-TVA-mCherry and AAV2-CAG-DIO-glycoprotein (1:2, 200 to

500 nl) into VIS (bregma, −3 mm; lateral, 2.5 mm; depth, 0.5 mm), RSP (bregma, −1.8 mm; lateral, 0.3 mm; depth, 0.5 mm), PTLp (bregma, −2.2 mm; lateral, 1.5 mm; depth, 0.5 mm), ACA (bregma, +0.5 mm; lateral, 0.3 mm; depth, 0.9 mm), PL/ILA (bregma, +2.2 mm; lateral, 0.3 mm; depth, 1.8 mm), or ORB (bregma, +2.8 mm; lateral, 1.3 mm; depth, 2 mm) of PV-, SST-, VIP-, and CaMKIIα-Cre mice. Two to three weeks later, RV-ΔG-EGFP^{+}EnvA (200 to 500 nl) was injected into the same site as AAV injection. The histology experiments were performed 7 days after RV injection.

For measuring the synaptic properties of long-range CC inputs, AAV-DJ-CaMKIIα-hChR2(H134R)-EYFP (150 to 500 nl) was injected into VIS, PTLp, RSP, ACA, ORB, or PL/ILA of PV-, SST-, and VIP-tdTomato mice. For measuring the synaptic properties of long-range TC inputs, AAV-DJ-CaMKIIα-hChR2(H134R)-EYFP (50 to 100 nl) was injected into LP/LD (bregma, −1.2 mm; lateral, 1 mm; depth, 2.8 mm) or MD (bregma, −1.4 mm; lateral, 0.4 mm; depth, 3.3 mm) of PV-, SST-, and VIP-tdTomato mice.

Histology

Mice were deeply anesthetized with isoflurane and immediately perfused with chilled 0.1 M phosphate-buffered saline (PBS) followed by 4% paraformaldehyde (w/v) in PBS. The brain was removed and postfixed overnight at 4°C. After fixation, the brain was placed in 30% sucrose (w/v) in PBS solution for 1 to 2 days at 4°C. After embedding and freezing, the brain was sectioned into 50-μm coronal slices using a cryostat. For fluorescence images, brain slices were washed with PBS for 0.5 hours and mounted with VECTASHIELD mounting medium with 4′,6-diamidino-2-phenylindole (DAPI). For immunohistochemistry for RG, brain slices were washed with PBS for 0.5 hours, permeabilized using PBST (0.3% Triton X-100 in PBS) for 10 min, and then incubated with blocking solution (5% normal goat serum in PBST) for 2 hours followed by primary antibody incubation overnight at 4°C using anti-RG mouse monoclonal antibody (1:100; MAB8727, Sigma-Aldrich). The next day, slices were washed five times with PBST and then incubated with secondary antibody (1:1000; goat anti-mouse immunoglobulin G, A-21235, Thermo Fisher Scientific) for 2 hours at room temperature. The slices were washed three times with PBST again and then mounted with VECTASHIELD mounting medium with DAPI. One of every three sections was imaged in the high-throughput slide scanners (Nanozoomer-2.0RS, Hamamatsu, or VS120, Olympus) for further processing. We also imaged selected example slices under a confocal microscope (Olympus FV-3000).

Three-dimensional reconstruction and quantification

A custom-written software package was used to analyze the digitized brain images. The analysis software consists of four modules: atlas rotation, image registration, signal detection, and quantification/visualization. The detailed method for the last three modules has been described previously (*30*).

Rotation module

The rotation module allows the 3D rotation of the Allen Mouse Brain Atlas by arbitrary angles to fit each sample. Anatomical landmarks were manually chosen to estimate the rotation angle. For estimating the rotation angle about the left-right axis, the most posterior slices containing the CA3 in each hemisphere were used. For estimating the rotation angle about the dorsal-ventral axis, the most anterior slice containing the anterior commissure crossing the midline and the most posterior slice containing the corpus callosum crossing the midline were used. The reference atlas was then rotated using these estimated angles to mimic the aberrant sectioning angle of the experimental brain.

Registration module

The registration module is a reference point–based image alignment software used to align images of brain sections to the rotated 3D reference atlas for further quantification and 3D reconstruction. First, reference points were chosen in both the atlas and the brain image. The module then applied geometric transformations of the brain section to optimize the match of the reference points between the brain image and the atlas. Following the transformation, the match between the image and the atlas was inspected, and further adjustments were made manually if necessary.

Detection module

The detection module for counting RV-labeled cells records the position of manually identified EGFP-labeled neurons in each digitized brain section image.

Quantification/visualization module

After detection and registration, signals were quantified across the whole brain and projected to the 3D reference atlas for better visualization. Since the number of labeled neurons varied across brains, the input from each region was quantified by dividing the number of labeled neurons found in that region by the total number of labeled neurons detected in the entire brain, with the exception of the injection site.

Slice recording

Mice were anaesthetized with 5% isoflurane. After decapitation, the brain was dissected rapidly and placed in ice-cold oxygenated *N*-methyl-D-glucamine (NMDG)–Hepes solution (93 mM NMDG, 2.5 mM KCl, 1.2 mM NaH_2PO_4, 30 mM $NaHCO_3$, 20 mM Hepes, 25 mM glucose, 5 mM sodium ascorbate, 2 mM thiourea, 3 mM sodium pyruvate, 10 mM $MgSO_4{\cdot}7H_2O$, 0.5 mM $CaCl_2{\cdot}2H_2O$, and 12 mM N-Acetyl-L-cysteine (NAC), at pH 7.4, adjusted with HCl), and coronal sections of brain slices were made with a vibratome. Slices (300 μm thick) were recovered in oxygenated NMDG-Hepes solution at 32°C for 10 min and then maintained in an incubation chamber with oxygenated standard artificial cerebrospinal fluid (ACSF) (125 mM NaCl, 3 mM KCl, 2 mM $CaCl_2$, 1 mM $MgCl_2$, 1.25 mM NaH_2PO_4, 1.3 mM sodium ascorbate, 26 mM $NaHCO_3$, and 10 mM glucose) at 30°C for 1 to 4 hours before recording.

Whole-cell recordings were made at 30°C in oxygenated standard ACSF. EPSPs were recorded using a potassium-based internal solution (135 mM K-gluconate, 5 mM KCl, 10 mM Hepes, 0.3 mM EGTA, 4 mM MgATP, 0.3 mM Na_2GTP, and 10 mM Na_2-phosphocreatine, at pH 7.3, adjusted with KOH, 290 to 300 mOsm). To activate ChR2, we used X-cite light-emitting diode (Lumen Dynamics Group), which was controlled by a stimulator (Master8) and bandpass-filtered at 419 to 465 nm (Semrock). Pulse trains of blue light (10 Hz, 5 ms) were delivered through a 40× 0.8 numerical aperture water immersion lens at a power of 1 to 2 mW. The resistance of the patch pipette was 3 to 5 megohm. The cells were excluded if the series resistance exceeded 40 megohm or varied by more than 20% during the recording period. Data were recorded with a MultiClamp 700B amplifier (Axon Instruments) filtered at 2 kHz and digitized with a Digidata 1322 (Axon instruments) at 10 kHz. Recordings were analyzed using custom software. To compare the response among different types of interneurons, the EPSP amplitude recorded from interneurons were normalized by the EPSP amplitude from nearby

Pyr neurons (distance of <100 μm). The EPSP amplitude of Pyr neurons was adjusted to 5 to 10 mV by adjusting the stimulation light intensity, whenever it is possible. In a few cases, the input is too weak to evoke 5-mV EPSP on Pyr neurons, we then used the maximum light intensity (8 mW) for stimulation. The PPR is measured by dividing the amplitude of the second EPSP into that of the first EPSP. For blocking the AMPA receptor–mediated EPSPs, CNQX (10 μM) was bath-applied.

Classification based on SVM classifier

SVM classification is implemented with the fitcsvm function in MATLAB statistics toolbox using linear kernel and a uniform prior. The data from well-defined bottom-up and top-down CC inputs were used to train the SVM classifier to reveal the decision boundaries for the classification of bottom-up and top-down inputs. We then use the trained SVM classifier to classify other CC and TC inputs. The classifier performance is computed using leave-one-out cross-validation with the data from well-defined bottom-up and top-down CC inputs. The classifier performance is also tested on 300 instances of shuffled labels to obtain the 95% confidence interval.

To reveal the link between the synaptic dynamics on different cortical interneurons and the directionality of long-range inputs, the data from all CC and TC inputs were used to train a SVM classifier. The direction of each input was classified by $\text{Classifier}_{\text{EPHYS}}$. The classifier performance is computed using leave-one-out cross-validation and tested on 300 instances of shuffled labels to obtain the 95% confidence interval.

Hierarchical organization analysis based on anatomic results

To quantify the hierarchical organization based on the input patterns of interneurons revealed by RV tracing, hierarchy index ($\text{HI}_{\text{ANATOMY}}$) for the connection from area i to area j was computed as

$$\text{HI}_{i\to j} = \frac{\text{VIP}_{i\to j} - \text{PV}_{i\to j}}{\text{VIP}_{i\to j} + \text{PV}_{i\to j}} \quad (1)$$

where $\text{VIP}_{i\to j}$ and $\text{PV}_{i\to j}$ are the input percentages (see the "Three-dimensional reconstruction and quantification" section) of VIP^+ and PV^+ neurons from $\text{input}_{i\to j}$, respectively.

We calculated the values of $\text{HI}_{\text{ANATOMY}}$ for both CC and TC inputs and trained the SVM classifier ($\text{Classifier}_{\text{ANATOMY}}$) with the $\text{HI}_{\text{ANATOMY}}$ values of well-defined bottom-up and top-down CC inputs (see the "Classification based on SVM classifier" section). $\text{Classifier}_{\text{ANATOMY}}$ was then used to classify other CC and TC inputs based on their $\text{HI}_{\text{ANATOMY}}$ values.

To evaluate the hierarchical position of cortical areas in the visual network based on their reciprocal connections, we computed the hierarchy score of each cortical area. The following algorithms were adapted from Harris *et al.* (*28*). Code and data files for hierarchical analyses are available through Github (https://github.com/SJTUZhangLab/HierarchyAnalysis). We defined the initial hierarchical score of a cortical area as

$$H_i^0 = \frac{1}{2}\left(\frac{1}{N_{\text{output}}}\sum_{n_o=1}^{N_{\text{output}}}\text{HI}_{\text{CC}_{i\to n_o}} - \frac{1}{N_{\text{input}}}\sum_{n_i=1}^{N_{\text{input}}}\text{HI}_{\text{CC}_{n_i\to i}}\right) \quad (2)$$

The first term, $\frac{1}{N_{\text{output}}}\sum_{n_o=1}^{N_{\text{output}}}\text{HI}_{\text{CC}_{i\to n_o}}$, is the averaged $\text{HI}_{\text{ANATOMY}}$ values of the CC outputs from area i and thus represents the hierarchical position of area i as a source. On the other hand, the second term, $-\frac{1}{N_{\text{input}}}\sum_{n_i=1}^{N_{\text{input}}}\text{HI}_{\text{CC}_{n_i\to i}}$, is the averaged $\text{HI}_{\text{ANATOMY}}$ values of the CC inputs to area i, showing the hierarchical position of area i as a target. The hierarchical position of a cortical area is the average between its hierarchical positions as source and target.

After we obtained the initial positions in the hierarchy, the hierarchy scores of all cortical areas are iterated until the fixed points are reached. To refine the hierarchy, we implemented a two-step iterative scheme

$$H_i^{n-1/2} = \frac{1}{2}\left[\frac{1}{N_{\text{output}}}\sum_{n_o=1}^{N_{\text{output}}}(\text{HI}_{\text{CC}_{i\to n_o}} + H_{n_o}^{n-1}) - \frac{1}{N_{\text{input}}}\sum_{n_i=1}^{N_{\text{input}}}(\text{HI}_{\text{CC}_{n_i\to i}} - H_{n_i}^{n-1})\right] \quad (3)$$

$$H_i^n = H_i^{n-1/2} - \frac{1}{K}\sum_{k=1}^{K}H_k^{n-1/2} \quad (4)$$

where n refers to iterative steps. Equation 3 refines the hierarchy score of area i based on the current hierarchy scores of its target and source areas. Equation 4 subtracts the hierarchy scores averaged over all areas to remove possible drifts. All the hierarchy scores reached the fixed points within 20 iterations (fig. S7). These final hierarchy scores indicated the hierarchy of cortical areas based on their reciprocal connections.

Next, we examined the effect of TC connections on the cortical hierarchy by adding the information of TC connections into the CC network. We defined the initial hierarchical score of a cortical area as

$$H_i^0 = \frac{1}{2}\left(\frac{1}{N_{\text{output}}}\sum_{n_o=1}^{N_{\text{output}}}\text{HI}_{\text{CC}_{i\to n_o}} - \frac{1}{N_{\text{input}}}\sum_{n_i=1}^{N_{\text{input}}}\text{HI}_{\text{CC+TC}_{n_i\to i}}\right) \quad (5)$$

Same as in Eq. 2, the first term is the averaged $\text{HI}_{\text{ANATOMY}}$ values of the CC outputs from cortical area i and thus represents the hierarchical position of cortical area i as a source. In addition, the second term, $-\frac{1}{N_{\text{input}}}\sum_{n_i=1}^{N_{\text{input}}}\text{HI}_{\text{CC+TC}_{n_i\to i}}$, is the averaged $\text{HI}_{\text{ANATOMY}}$ values of both CC and TC inputs to cortical area i, showing the hierarchical position of cortical area i as a target. Thus, the hierarchical position of a cortical area is the average between its hierarchical positions as source and target. Since the thalamic areas are always the source in the TC connections, the initial hierarchy score of each thalamic area i is defined by the averaged $\text{HI}_{\text{ANATOMY}}$ values of the TC outputs from thalamic area i

$$H_i^0 = \frac{1}{N_{\text{output}}}\sum_{n_o=1}^{N_{\text{output}}}\text{HI}_{\text{TC}_{i\to n_o}} \quad (6)$$

Once the initial hierarchy scores of the cortical and thalamic areas are obtained, all the scores are iterated until the fixed points are reached (<20 iterations) (fig. S7) using the following functions for cortical (Eqs. 7 and 9) and thalamic areas (Eqs. 8 and 9), respectively

$$H_i^{n-1/2} = \frac{1}{2}\left[\frac{1}{N_{\text{output}}}\sum_{n_o=1}^{N_{\text{output}}}(\text{HI}_{\text{CC}_{i\to n_o}} + H_{n_o}^{n-1}) - \frac{1}{N_{\text{input}}}\sum_{n_i=1}^{N_{\text{input}}}(\text{HI}_{\text{CC+TC}_{n_i\to i}} - H_{n_i}^{n-1})\right] \quad (7)$$

$$H_i^{n-1/2} = \frac{1}{N_{\text{output}}}\sum_{n_o=1}^{N_{\text{output}}}(\text{HI}_{\text{TC}_{i\to n_o}} + H_{n_o}^{n-1}) \quad (8)$$

$$H_i^n = H_i^{n-1/2} - \frac{1}{K}\sum_{k=1}^{K} H_k^{n-1/2} \quad (9)$$

Last, we examined whether the hierarchical information provided by TC inputs is consistent with CC inputs by comparing the hierarchy predicted by TC connections only with the one predicted by both CC and TC connections. The initial hierarchy score of cortical area i is defined by the averaged $HI_{ANATOMY}$ values of the TC inputs to cortical area i

$$H_i^0 = \frac{1}{N_{input}}\sum_{n_i=1}^{N_{input}} HI_{TC_{n_i \to i}} \quad (10)$$

The initial hierarchy score of each thalamic area i is defined by the averaged $HI_{ANATOMY}$ values of the outputs from thalamic area i

$$H_i^0 = \frac{1}{N_{output}}\sum_{n_o=1}^{N_{output}} HI_{TC_{i \to n_o}} \quad (11)$$

Once the initial hierarchy scores of the cortical and thalamic areas are obtained, all the scores are iterated using the following functions for cortial (Eqs. 12 and 14) and thalamic areas (Eqs. 13 and 14), respectively

$$H_i^{n-1/2} = \frac{1}{N_{input}}\sum_{n_i=1}^{N_{input}} (HI_{TC_{n_i \to i}} - H_{n_i}^{n-1}) \quad (12)$$

$$H_i^{n-1/2} = \frac{1}{N_{output}}\sum_{n_o=1}^{N_{output}} (HI_{TC_{i \to n_o}} + H_{n_o}^{n-1}) \quad (13)$$

$$H_i^n = H_i^{n-1/2} - \frac{1}{K}\sum_{k=1}^{K} H_k^{n-1/2} \quad (14)$$

we found that the hierarchy scores of each area oscillate between two fixed values in consecutive iterations after iterating for 20 times, but the global hierarchy scores (see Eqs. 15 to 17 below) reach a fixed value (<20 iterations) (fig. S7). We then used the hierarchy scores generated by the last iteration (50th iteration).

In this way, we obtained three versions of hierarchy constructed from (i) CC connections only, (ii) both CC and TC connections, and (iii) TC connections only. To examine the self-consistency of the hierarchy, we compared the global hierarchy scores of the three different versions of hierarchy. The global hierarchy scores were computed as

$$z(H_i - H_j) = \frac{(H_i - H_j) - \langle H_i - H_j \rangle_{i,j}}{\sqrt{\cdot[(H_i - H_j) - \langle H_i - H_j \rangle_{i,j}]^2}} \quad (15)$$

$$z(HI_{i \to j}) = \frac{HI_{i \to j} - \langle HI_{i \to j} \rangle_{i,j}}{\sqrt{\cdot(HI_{i \to j} - \langle HI_{i \to j} \rangle_{i,j})^2}} \quad (16)$$

$$h = \langle z(H_i - H_j) \times z(HI_{i \to j}) \rangle_{i,j} \quad (17)$$

First, we calculated the z score of the difference between hierarchy scores (Eq. 15) and the z score of the hierarchy index (Eq. 16). Next, the global hierarchy score h was calculated as the covariance between the two vectors of z scores (Eq. 17). Thus, the global hierarchy score is the correlation between the hierarchy-score difference and the hierarchy index. The global hierarchy score of perfectly self-consistent hierarchy is 1.

To assess the significance of the hierarchy levels of cortical and thalamic areas, we generated 500 sampled connectivity data of the same size via bootstrapping and then computed the hierarchy scores of the cortical and thalamic areas using the bootstrapped connectivity data, following the method of Siegle *et al.* (*23*). We found that in the hierarchy constructed from both CC and TC connections, only the hierarchy scores of thalamic areas SMT and AM/AD/AV/IAD are not significantly different ($P = 0.74$, Wilcoxon signed-rank test). See table S1 for anatomical abbreviations. The hierarchy scores of all other structures are significantly different ($P < 0.03$, Wilcoxon signed-rank test).

Global hierarchy score of shuffled connectomes

To demonstrate that the cortical and thalamic areas in the visual network have significant hierarchical organization, we generated shuffled connectivity data for the connection patterns, computed the global hierarchy scores, and compared the global hierarchy scores of the shuffled connectivity to that of the observed connectivity, adapting from the method of Harris *et al.* (*28*). The shuffled connectivity is constructed by randomly rearranging sources and targets, while preserving the HI values and the distributions of source and target areas. We generated 300 versions of shuffled connectivity data and calculated their global hierarchy scores using the algorithms described in the previous section. The medians of the shuffled distributions provide an estimate of the lower bound of this score (0.54 for CC, 0.53 for CC + TC, and 0.72 for TC; Fig. 3C and fig. S8). For the hierarchy based on both CC and TC connections, shuffling either CC or TC connections induced significant decrease of the global hierarchy scores ($P < 7 \times 10^{-51}$, Wilcoxon signed-rank test), indicating that both connections provided important information for the hierarchical organization in the visual network.

Hierarchical organization analysis based on physiological recordings

To compare the hierarchy derived from physiological recording with the one derived from anatomic data, the hierarchy index (HI_{EPHYS}) for the connection from area i to area j was computed using Eq. 1, but $VIP_{i \to j}$ and $PV_{i \to j}$ are the input strengths (see the "Slice recording" section) of VIP^+ and PV^+ neurons from $input_{i \to j}$. We calculated the values of HI_{EPHYS} for both CC and TC inputs and trained the SVM classifier ($Classifier_{EPHYS}$) with the HI_{EPHYS} from well-defined bottom-up and top-down CC inputs (see the "Classification based on SVM classifier" section). $Classifier_{EPHYS}$ was then used to classify other CC and TC inputs based on their HI_{EPHYS} values.

Using the same algorithms as in the "Hierarchical organization analysis based on anatomic results" section, we obtained the cortical hierarchy constructed from the CC connections based on their HI_{EPHYS} and compared it with the one based on the $HI_{ANATOMY}$ (Fig. 5E). PTLp was excluded in this analysis because of the lack of the HI_{EPHYS} of the connections between PTLp and VIS and the connections between PTLp and ACA.

Statistical analysis

All statistical tests and data analysis were performed using MATLAB. All statistical tests were two-sided. Data were expressed as means ± SEMs in figures and text. Statistical significance was tested with the Wilcoxon rank-sum test and Wilcoxon signed-rank test, with a 95% confidence interval. Sample size was not statistically predetermined but based on previous publications of similar studies (*16*, *30*, *43*, *45*). The "*n*" number for each experiment is provided in the text and figure legends.

SUPPLEMENTARY MATERIALS

Supplementary material for this article is available at http://advances.sciencemag.org/cgi/content/full/7/20/eabf5676/DC1

View/request a protocol for this paper from *Bio-protocol*.

REFERENCES AND NOTES

1. A. Paul, M. Crow, R. Raudales, M. He, J. Gillis, Z. J. Huang, Transcriptional architecture of synaptic communication delineates GABAergic neuron identity. *Cell* **171**, 522–539.e20 (2017).
2. B. Tasic, Z. Yao, L. T. Graybuck, K. A. Smith, T. N. Nguyen, D. Bertagnolli, J. Goldy, E. Garren, M. N. Economo, S. Viswanathan, O. Penn, T. Bakken, V. Menon, J. Miller, O. Fong, K. E. Hirokawa, K. Lathia, C. Rimorin, M. Tieu, R. Larsen, T. Casper, E. Barkan, M. Kroll, S. Parry, N. V. Shapovalova, D. Hirschstein, J. Pendergraft, H. A. Sullivan, T. K. Kim, A. Szafer, N. Dee, P. Groblewski, I. Wickersham, A. Cetin, J. A. Harris, B. P. Levi, S. M. Sunkin, L. Madisen, T. L. Daigle, L. Looger, A. Bernard, J. Phillips, E. Lein, M. Hawrylycz, K. Svoboda, A. R. Jones, C. Koch, H. Zeng, Shared and distinct transcriptomic cell types across neocortical areas. *Nature* **563**, 72–78 (2018).
3. X. Jiang, S. Shen, C. R. Cadwell, P. Berens, F. Sinz, A. S. Ecker, S. Patel, A. S. Tolias, Principles of connectivity among morphologically defined cell types in adult neocortex. *Science* **350**, aac9462 (2015).
4. Y. Kim, G. R. Yang, K. Pradhan, K. U. Venkataraju, M. Bota, L. C. G. Del Molino, G. Fitzgerald, K. Ram, M. He, J. M. Levine, P. Mitra, Z. J. Huang, X.-J. Wang, P. Osten, Brain-wide maps reveal stereotyped cell-type-based cortical architecture and subcortical sexual dimorphism. *Cell* **171**, 456–469.e422 (2017).
5. S. Lee, I. Kruglikov, Z. J. Huang, G. Fishell, B. Rudy, A disinhibitory circuit mediates motor integration in the somatosensory cortex. *Nat. Neurosci.* **16**, 1662–1670 (2013).
6. C. K. Pfeffer, M. Xue, M. He, Z. J. Huang, M. Scanziani, Inhibition of inhibition in visual cortex: The logic of connections between molecularly distinct interneurons. *Nat. Neurosci.* **16**, 1068–1076 (2013).
7. H. J. Pi, B. Hangya, D. Kvitsiani, J. I. Sanders, Z. J. Huang, A. Kepecs, Cortical interneurons that specialize in disinhibitory control. *Nature* **503**, 521–524 (2013).
8. G. Fishell, A. Kepecs, Interneuron types as attractors and controllers. *Annu. Rev. Neurosci.* **43**, 1–30 (2020).
9. K. D. Harris, G. M. G. Shepherd, The neocortical circuit: Themes and variations. *Nat. Neurosci.* **18**, 170–181 (2015).
10. J. S. Isaacson, M. Scanziani, How inhibition shapes cortical activity. *Neuron* **72**, 231–243 (2011).
11. R. Tremblay, S. Lee, B. Rudy, GABAergic interneurons in the neocortex: From cellular properties to circuits. *Neuron* **91**, 260–292 (2016).
12. S. J. Cruikshank, T. J. Lewis, B. W. Connors, Synaptic basis for intense thalamocortical activation of feedforward inhibitory cells in neocortex. *Nat. Neurosci.* **10**, 462–468 (2007).
13. R. D. D'Souza, A. M. Meier, P. Bista, Q. Wang, A. Burkhalter, Recruitment of inhibition and excitation across mouse visual cortex depends on the hierarchy of interconnecting areas. *eLife* **5**, e19332 (2016).
14. N. J. Priebe, D. Ferster, Direction selectivity of excitation and inhibition in simple cells of the cat primary visual cortex. *Neuron* **45**, 133–145 (2005).
15. M. Wehr, A. M. Zador, Balanced inhibition underlies tuning and sharpens spike timing in auditory cortex. *Nature* **426**, 442–446 (2003).
16. S. Zhang, M. Xu, T. Kamigaki, J. P. Hoang Do, W.-C. Chang, S. Jenvay, K. Miyamichi, L. Luo, Y. Dan, Long-range and local circuits for top-down modulation of visual cortex processing. *Science* **345**, 660–665 (2014).
17. T. A. Coogan, A. Burkhalter, Hierarchical organization of areas in rat visual cortex. *J. Neurosci.* **13**, 3749–3772 (1993).
18. D. J. Felleman, D. C. Van Essen, Distributed hierarchical processing in the primate cerebral cortex. *Cereb. Cortex* **1**, 1–47 (1991).
19. E. Froudarakis, P. G. Fahey, J. Reimer, S. M. Smirnakis, E. J. Tehovnik, A. S. Tolias, The visual cortex in context. *Annu. Rev. Vis. Sci.* **5**, 317–339 (2019).
20. L. L. Glickfeld, S. R. Olsen, Higher-order areas of the mouse visual cortex. *Annu. Rev. Vis. Sci.* **3**, 251–273 (2017).
21. J. Hegde, D. J. Felleman, Reappraising the functional implications of the primate visual anatomical hierarchy. *Neuroscientist* **13**, 416–421 (2007).
22. J. J. Nassi, E. M. Callaway, Parallel processing strategies of the primate visual system. *Nat. Rev. Neurosci.* **10**, 360–372 (2009).
23. J. H. Siegle, X. Jia, S. Durand, S. Gale, C. Bennett, N. Graddis, G. Heller, T. K. Ramirez, H. Choi, J. A. Luviano, P. A. Groblewski, R. Ahmed, A. Arkhipov, A. Bernard, Y. N. Billeh, D. Brown, M. A. Buice, N. Cain, S. Caldejon, L. Casal, A. Cho, M. Chvilicek, T. C. Cox, K. Dai, D. J. Denman, S. E. J. de Vries, R. Dietzman, L. Esposito, C. Farrell, D. Feng, J. Galbraith, M. Garrett, E. C. Gelfand, N. Hancock, J. A. Harris, R. Howard, B. Hu, R. Hytnen, R. Iyer, E. Jessett, K. Johnson, I. Kato, J. Kiggins, S. Lambert, J. Lecoq, P. Ledochowitsch, J. H. Lee, A. Leon, Y. Li, E. Liang, F. Long, K. Mace, J. Melchior, D. Millman, T. Mollenkopf, C. Nayan, L. Ng, K. Ngo, T. Nguyen, P. R. Nicovich, K. North, G. K. Ocker, D. Ollerenshaw, M. Oliver, M. Pachitariu, J. Perkins, M. Reding, D. Reid, M. Robertson, K. Ronellenfitch, S. Seid, C. Slaughterbeck, M. Stoecklin, D. Sullivan, B. Sutton, J. Swapp, C. Thompson, K. Turner, W. Wakeman, J. D. Whitesell, D. Williams, A. Williford, R. Young, H. Zeng, S. Naylor, J. W. Phillips, R. C. Reid, S. Mihalas, S. R. Olsen, C. Koch, Survey of spiking in the mouse visual system reveals functional hierarchy. *Nature* **592**, 86–92 (2021).
24. B. J. Hunnicutt, B. R. Long, D. Kusefoglu, K. J. Gertz, H. Zhong, T. Mao, A comprehensive thalamocortical projection map at the mesoscopic level. *Nat. Neurosci.* **17**, 1276–1285 (2014).
25. S. W. Oh, J. A. Harris, L. Ng, B. Winslow, N. Cain, S. Mihalas, Q. Wang, C. Lau, L. Kuan, A. M. Henry, M. T. Mortrud, B. Ouellette, T. N. Nguyen, S. A. Sorensen, C. R. Slaughterbeck, W. Wakeman, Y. Li, D. Feng, A. Ho, E. Nicholas, K. E. Hirokawa, P. Bohn, K. M. Joines, H. Peng, M. J. Hawrylycz, J. W. Phillips, J. G. Hohmann, P. Wohnoutka, C. R. Gerfen, C. Koch, A. Bernard, C. Dang, A. R. Jones, H. Zeng, A mesoscale connectome of the mouse brain. *Nature* **508**, 207–214 (2014).
26. B. Zingg, H. Hintiryan, L. Gou, M. Y. Song, M. Bay, M. S. Bienkowski, N. N. Foster, S. Yamashita, I. Bowman, A. W. Toga, H. W. Dong, Neural networks of the mouse neocortex. *Cell* **156**, 1096–1111 (2014).
27. E. M. Callaway, L. Q. Luo, Monosynaptic circuit tracing with glycoprotein-deleted rabies viruses. *J. Neurosci.* **35**, 8979–8985 (2015).
28. J. A. Harris, S. Mihalas, K. E. Hirokawa, J. D. Whitesell, H. Choi, A. Bernard, P. Bohn, S. Caldejon, L. Casal, A. Cho, A. Feiner, D. Feng, N. Gaudreault, C. R. Gerfen, N. Graddis, P. A. Groblewski, A. M. Henry, A. Ho, R. Howard, J. E. Knox, L. Kuan, X. Kuang, J. Lecoq, P. Lesnar, Y. Li, J. Luviano, S. McConoughey, M. T. Mortrud, M. Naeemi, L. Ng, S. W. Oh, B. Ouellette, E. Shen, S. A. Sorensen, W. Wakeman, Q. Wang, Y. Wang, A. Williford, J. W. Phillips, A. R. Jones, C. Koch, H. Zeng, Hierarchical organization of cortical and thalamic connectivity. *Nature* **575**, 195–202 (2019).
29. L. Kuan, Y. Li, C. Lau, D. Feng, A. Bernard, S. M. Sunkin, H. Zeng, C. Dang, M. Hawrylycz, L. Ng, Neuroinformatics of the allen mouse brain connectivity atlas. *Methods* **73**, 4–17 (2015).
30. S. Zhang, M. Xu, W. C. Chang, C. Ma, J. P. Hoang Do, D. Jeong, T. Lei, J. L. Fan, Y. Dan, Organization of long-range inputs and outputs of frontal cortex for top-down control. *Nat. Neurosci.* **19**, 1733–1742 (2016).
31. M. M. Halassa, S. M. Sherman, Thalamocortical circuit motifs: A general framework. *Neuron* **103**, 762–770 (2019).
32. E. G. Jones, *The Thalamus* (Cambridge Univ. Press, ed. 2, 2007).
33. L. Petreanu, T. Mao, S. M. Sternson, K. Svoboda, The subcellular organization of neocortical excitatory connections. *Nature* **457**, 1142–1145 (2009).
34. F. Hu, T. Kamigaki, Z. Zhang, S. Zhang, U. Dan, Y. Dan, Prefrontal corticotectal neurons enhance visual processing through the superior colliculus and pulvinar thalamus. *Neuron* **104**, 1141–1152.e4 (2019).
35. D. P. Collins, P. G. Anastasiades, J. J. Marlin, A. G. Carter, Reciprocal circuits linking the prefrontal cortex with dorsal and ventral thalamic nuclei. *Neuron* **98**, 366–379.e4 (2018).
36. K. Delevich, J. Tucciarone, Z. J. Huang, B. Li, The mediodorsal thalamus drives feedforward inhibition in the anterior cingulate cortex via parvalbumin interneurons. *J. Neurosci.* **35**, 5743–5753 (2015).
37. L. I. Schmitt, R. D. Wimmer, M. Nakajima, M. Happ, S. Mofakham, M. M. Halassa, Thalamic amplification of cortical connectivity sustains attentional control. *Nature* **545**, 219–223 (2017).
38. A. L. Juavinett, E. J. Kim, H. C. Collins, E. M. Callaway, A systematic topographical relationship between mouse lateral posterior thalamic neurons and their visual cortical projection targets. *J. Comp. Neurol.* **528**, 95–107 (2020).
39. N. J. Audette, J. Urban-Ciecko, M. Matsushita, A. L. Barth, POm thalamocortical input drives layer-specific microcircuits in somatosensory cortex. *Cereb. Cortex* **28**, 1312–1328 (2018).
40. L. A. DeNardo, D. S. Berns, K. DeLoach, L. Luo, Connectivity of mouse somatosensory and prefrontal cortex examined with trans-synaptic tracing. *Nat. Neurosci.* **18**, 1687–1697 (2015).
41. Y. Han, J. M. Kebschull, R. A. A. Campbell, D. Cowan, F. Imhof, A. M. Zador, T. D. Mrsic-Flogel, The logic of single-cell projections from visual cortex. *Nature* **556**, 51–56 (2018).
42. E. J. Kim, A. L. Juavinett, E. M. Kyubwa, M. W. Jacobs, E. M. Callaway, Three types of cortical layer 5 neurons that differ in brain-wide connectivity and function. *Neuron* **88**, 1253–1267 (2015).
43. S. Ährlund-Richter, Y. Xuan, J. A. van Lunteren, H. Kim, C. Ortiz, I. P. Dorocic, K. Meletis, M. Carlén, A whole-brain atlas of monosynaptic input targeting four different cell types in the medial prefrontal cortex of the mouse. *Nat. Neurosci.* **22**, 657–668 (2019).
44. Q. Sun, X. Li, M. Ren, M. Zhao, Q. Zhong, Y. Ren, P. Luo, H. Ni, X. Zhang, C. Zhang, J. Yuan, A. Li, M. Luo, H. Gong, Q. Luo, A whole-brain map of long-range inputs to GABAergic interneurons in the mouse medial prefrontal cortex. *Nat. Neurosci.* **22**, 1357–1370 (2019).

45. N. R. Wall, M. de la Parra, J. M. Sorokin, H. Taniguchi, Z. J. Huang, E. M. Callaway, Brain-wide maps of synaptic input to cortical interneurons. *J. Neurosci.* **36**, 4000–4009 (2016).
46. A. Nelson, R. Mooney, The basal forebrain and motor cortex provide convergent yet distinct movement-related inputs to the auditory cortex. *Neuron* **90**, 635–648 (2016).
47. H. Adesnik, W. Bruns, H. Taniguchi, Z. J. Huang, M. Scanziani, A neural circuit for spatial summation in visual cortex. *Nature* **490**, 226–231 (2012).
48. B. S. Sermet, P. Truschow, M. Feyerabend, J. M. Mayrhofer, T. B. Oram, O. Yizhar, J. F. Staiger, C. C. H. Petersen, Pathway-, layer- and cell-type-specific thalamic input to mouse barrel cortex. *eLife* **8**, e52665 (2019).
49. R. Hattori, B. Danskin, Z. Babic, N. Mlynaryk, T. Komiyama, Area-specificity and plasticity of history-dependent value coding during learning. *Cell* **177**, 1858–1872.e15 (2019).
50. R. Hattori, K. V. Kuchibhotla, R. C. Froemke, T. Komiyama, Functions and dysfunctions of neocortical inhibitory neuron subtypes. *Nat. Neurosci.* **20**, 1199–1208 (2017).
51. A. J. Peters, S. X. Chen, T. Komiyama, Emergence of reproducible spatiotemporal activity during motor learning. *Nature* **510**, 263–267 (2014).
52. J. K. Schiavo, S. Valtcheva, C. J. Bair-Marshall, S. C. Song, K. A. Martin, R. C. Froemke, Innate and plastic mechanisms for maternal behaviour in auditory cortex. *Nature* **587**, 426–431 (2020).
53. Y. Xin, L. Zhong, Y. Zhang, T. Zhou, J. Pan, N.-L. Xu, Sensory-to-category transformation via dynamic reorganization of ensemble structures in mouse auditory cortex. *Neuron* **103**, 909–921.e6 (2019).
54. H. Makino, T. Komiyama, Learning enhances the relative impact of top-down processing in the visual cortex. *Nat. Neurosci.* **18**, 1116–1122 (2015).
55. N. A. Steinmetz, P. Zatka-Haas, M. Carandini, K. D. Harris, Distributed coding of choice, action and engagement across the mouse brain. *Nature* **576**, 266–273 (2019).
56. K. D. Harris, T. D. Mrsic-Flogel, Cortical connectivity and sensory coding. *Nature* **503**, 51–58 (2013).
57. M. Dipoppa, A. Ranson, M. Krumin, M. Pachitariu, M. Carandini, K. D. Harris, Vision and locomotion shape the interactions between neuron types in mouse visual cortex. *Neuron* **98**, 602–615.e8 (2018).
58. K. V. Kuchibhotla, J. V. Gill, G. W. Lindsay, E. S. Papadoyannis, R. E. Field, T. A. H. Sten, K. D. Miller, R. C. Froemke, Parallel processing by cortical inhibition enables context-dependent behavior. *Nat. Neurosci.* **20**, 62–71 (2017).
59. M. He, J. Tucciarone, S. H. Lee, M. J. Nigro, Y. Kim, J. M. Levine, S. M. Kelly, I. Krugikov, P. Wu, Y. Chen, L. Gong, Y. Hou, P. Osten, B. Rudy, Z. J. Huang, Strategies and tools for combinatorial targeting of GABAergic neurons in mouse cerebral cortex. *Neuron* **92**, 555 (2016).
60. M. J. Yetman, E. Washburn, J. H. Hyun, F. Osakada, Y. Hayano, H. Zeng, E. M. Callaway, H. B. Kwon, H. Taniguchi, Intersectional monosynaptic tracing for dissecting subtype-specific organization of GABAergic interneuron inputs. *Nat. Neurosci.* **22**, 492–502 (2019).
61. R. Yuste, M. Hawrylycz, N. Aalling, A. Aguilar-Valles, D. Arendt, R. Armañanzas, G. A. Ascoli, C. Bielza, V. Bokharaie, T. B. Bergmann, I. Bystron, M. Capogna, Y. J. Chang, A. Clemens, C. P. J. de Kock, J. DeFelipe, S. E. Dos Santos, K. Dunville, D. Feldmeyer, R. Fiáth, G. J. Fishell, A. Foggetti, X. Gao, P. Ghaderi, N. A. Goriounova, O. Güntürkün, K. Hagihara, V. J. Hall, M. Helmstaedter, S. Herculano-Houzel, M. M. Hilscher, H. Hirase, J. Hjerling-Leffler, R. Hodge, J. Huang, R. Huda, K. Khodosevich, O. Kiehn, H. Koch, E. S. Kuebler, M. Kühnemund, P. Larrañaga, B. Lelieveldt, E. L. Louth, J. H. Lui, H. D. Mansvelder, O. Marin, J. Martinez-Trujillo, H. M. Chameh, A. N. Mohapatra, H. Munguba, M. Nedergaard, P. Němec, N. Ofer, U. G. Pfisterer, S. Pontes, W. Redmond, J. Rossier, J. R. Sanes, R. H. Scheuermann, E. Serrano-Saiz, J. F. Staiger, P. Somogyi, G. Tamás, A. S. Tolias, M. A. Tosches, M. T. García, C. Wozny, T. V. Wuttke, Y. Liu, J. Yuan, H. Zeng, E. Lein, A community-based transcriptomics classification and nomenclature of neocortical cell types. *Nat. Neurosci.* **23**, 1456–1468 (2020).
62. N. Chen, H. Sugihara, M. Sur, An acetylcholine-activated microcircuit drives temporal dynamics of cortical activity. *Nat. Neurosci.* **18**, 892–902 (2015).
63. Y. Fu, J. M. Tucciarone, J. S. Espinosa, N. Sheng, D. P. Darcy, R. A. Nicoll, Z. J. Huang, M. P. Stryker, A cortical circuit for gain control by behavioral state. *Cell* **156**, 1139–1152 (2014).
64. L. Pinto, M. J. Goard, D. Estandian, M. Xu, A. C. Kwan, S. H. Lee, T. C. Harrison, G. Feng, Y. Dan, Fast modulation of visual perception by basal forebrain cholinergic neurons. *Nat. Neurosci.* **16**, 1857–1863 (2013).
65. S. J. Cruikshank, H. Urabe, A. V. Nurmikko, B. W. Connors, Pathway-specific feedforward circuits between thalamus and neocortex revealed by selective optical stimulation of axons. *Neuron* **65**, 230–245 (2010).

Acknowledgments: We thank J. Lu, X. Chen, and M. Poo for critical reading of our manuscript and M. Qin, D. Liu, Y. Miao, Z. Chen, and Z. Deng for the technique help. **Funding:** This study was supported by grants from the National Natural Science Foundation of China (31871051, 31900711, and 31930050), the Science and Technology Commission of Shanghai Municipality (18JC1420302), and the innovative research team of high-level local universities in Shanghai.
Author contributions: G.M., M.X., and S.Z. designed the experiments. G.M. and Y.L. performed most of the experiments. M.X. and Z.X. wrote the software for data analysis. L.W. and W.P. prepared AAV vectors for rabies virus–based retrograde tracing and optogenetic activation. K.S., W.P., and Z.T. collected the digital images of brain tissue sections. L.W., K.S., Y.W., W.P., X.L., and Z.W. performed part of the brain tissue sectioning and the digital image analysis. S.J. and F.X. helped with RV tracing experiment. C.T.L. and T.X. contributed to the experiment design and paper editing. G.M., Y.L., M.X., and S.Z. wrote the manuscript. **Competing interests:** The authors declare that they have no competing interests. **Data and materials availability:** All data needed to evaluate the conclusions in the paper are present in the paper and/or the Supplementary Materials. Code and data files for hierarchical analyses are available through Github (https://github.com/SJTUZhangLab/HierarchyAnalysis). Additional data related to this paper may be requested from the authors.

Submitted 4 November 2020
Accepted 26 March 2021
Published 14 May 2021
10.1126/sciadv.abf5676

Citation: G. Ma, Y. Liu, L. Wang, Z. Xiao, K. Song, Y. Wang, W. Peng, X. Liu, Z. Wang, S. Jin, Z. Tao, C. T. Li, T. Xu, F. Xu, M. Xu, S. Zhang, Hierarchy in sensory processing reflected by innervation balance on cortical interneurons. *Sci. Adv.* **7**, eabf5676 (2021).